Science Arts & Métiers (SAM)

is an open access repository that collects the work of Arts et Métiers Institute of Technology researchers and makes it freely available over the web where possible.

This is an author-deposited version published in: https://sam.ensam.eu
Handle ID: .http://hdl.handle.net/10985/22205

To cite this version :

Pouya TAJDARY, Léo MORIN, Liliana ROMERO-RESENDIZ, Maysam B. GORJI, Chedly BRAHAM, Gonzalo GONZALEZ - Analysis of shear ductile damage in forming processes using a micromechanical model with void shape effects - International Journal of Solids and Structures - Vol. 248, p.111640 - 2022

Any correspondence concerning this service should be sent to the repository Administrator : scienceouverte@ensam.eu

Arts et Métiers Institute of Technology

Analysis of shear ductile damage in forming processes using a micromechanical model with void shape effects

Pouya Tajdary [a], Léo Morin [a,*], Liliana Romero-Resendiz [b], Maysam B. Gorji [c,d], Chedly Braham [a], Gonzalo Gonzalez [b]

[a] Laboratoire PIMM, Arts et Metiers Institute of Technology, CNRS, Cnam, HESAM Universite, 151 boulevard de l'Hopital, 75013 Paris, France
[b] Instituto de Investigaciones en Materiales, Universidad Nacional Autónoma de México, Circuito Ext S/N, Cd. Universitaria, 04510, Mexico City, Mexico
[c] Impact and Crashworthiness Laboratory, Department of Mechanical Engineering, Massachusetts Institute of Technology, Cambridge MA, USA
[d] Exponent Inc., Engineering and Scientific Consulting, Menlo Park, CA, USA

A B S T R A C T

The aim of this work is to investigate and predict ductile failure in forming processes. Experimental results of deep drawing and corrugation processing on aluminum alloys suggest that in some cases failure can be due to shear-dominated loadings. In order to simulate numerically failure during forming, we use the micromechanical Madou–Leblond model, which permits to account for void shape effects that are important under shear loadings. In the case of deep drawing, the model is able to reproduce failure either due to bottom or shear cracks, depending on the processing conditions. In the case of corrugation processing, the model reproduces accurately the occurrence of failure as well as the crack shape. Comparisons with the GTN model show the importance of void shape effects upon failure.

1. Introduction

The accurate simulation of metal forming processes is of paramount importance to increase industrial performances either by reducing the manufacturing time or improving the quality of the products. The simulation of forming, alternatively called virtual metal forming, has known important successes due to the use of advanced material laws and the development of the finite element method with geometric nonlinearity (Banabic, 2010; Ablat and Qattawi, 2017). Among the remaining challenges, the numerical simulation of damage, caused by large plastic strains during metal forming processing, is important to provide defect-free specimens (Saanouni, 2006; Tekkaya et al., 2020).

The ductile failure of metals is generally due to the successive nucleation, growth and coalescence of micro-voids (Benzerga and Leblond, 2010; Benzerga et al., 2016; Pineau et al., 2016). It is now commonly accepted that void nucleation can occur by decohesion at second-phase particles–matrix interface or by particle cracking. Once voids are nucleated, plastic flow will promote the growth of these voids, which is accelerated by the stress triaxiality. Then important void growth is usually followed by void coalescence which can take place in a variety of modes, the most dominant one being coalescence by internal necking (Benzerga, 2002). Recent experimental works have shown that ductile failure can also occur under combined tension and shear, and notably with shear-dominated loadings (Barsoum and Faleskog, 2007; Dunand and Mohr, 2011b,a; Ghahremaninezhad and Ravi-Chandar, 2013; Haltom et al., 2013; Roth et al., 2018; Grolleau et al., 2022). In such cases, void growth is limited and the macroscopic softening is attributed to changes of the void shape and orientation, notably the flattening of voids subjected to shear.

The modeling of ductile damage is based on either uncoupled fracture criteria, such as the Hosford–Coulomb fracture model (see e.g. Gorji and Mohr (2018), Nahrmann and Matzenmiller (2021) and Zhang et al. (2022)), or coupled damage models. In the first approach, the damage parameter does not affect the material behavior, whereas in the second approach damage is coupled with elastic and/or plastic properties (Tekkaya et al., 2020). In the coupled damage approach, which is generally referred to as the local approach of fracture, the modeling of ductile failure is essentially based on a detailed and physically-based description of the local rupture process zone (Besson, 2010). Within this framework, two main approaches permit to describe ductile damage evolution:

(1) *Continuum damage mechanics (CDM) models* are based on a thermodynamical framework following Lemaitre (1985)'s pioneering work. In this approach, damage is taken into account through a phenomenological internal damage state variable (which can

be scalar or tensorial), which affects both the elastic behavior and the plastic flow. This class of models is referred to as phenomenological as their development is essentially based on macroscopic considerations. The evolution of the damage variable is driven by the elastic energy release rate, in which the effect of triaxiality is accounted for. The thermodynamical consistency of CDM models together with their numerous extensions (such as damage anisotropy, plastic compressibility, kinematic hardening, strain rate effects, etc.) make this approach attractive, from a numerical point of view, for the simulation of ductile damage (Bonora, 1997; Saanouni et al., 2000).

(2) *Micromechanical type models* are based on a local description of the physical mechanisms of ductile failure, following mainly (Gurson, 1977)'s seminal work.[1] Gurson's model is based on the limit-analysis of a hollow sphere (with a rigid-plastic matrix) subjected to conditions of homogeneous boundary strain rate. This model is composed of a macroscopic yield criterion and flow rule which accounts for the presence of voids through the porosity. It is supplemented by an evolution equation for the porosity, which acts as a damage parameter in this model (although it can decrease in compression). Since it is limited to the description of void growth in isotropic solids, numerous extensions have permitted to account for more realistic situations including plastic anisotropy (Benzerga and Besson, 2001), void shape effects (Madou and Leblond, 2012a), kinematic hardening (Morin et al., 2017b), coalescence (Benzerga and Leblond, 2014), shear damage (Nahshon and Hutchinson, 2008), etc. This approach has met, in both its original and improved forms, considerable success in the reproduction of experimental tests of failure of ductile materials (Benzerga et al., 2016; Pineau et al., 2016).

In terms of numerical simulation of damage evolution during sheet metal forming, most of the works have considered continuum damage mechanics (see e.g. Saanouni et al. (2000), Teixeira et al. (2006), Saanouni (2008), Soyarslan and Tekkaya (2010), Saxena and Dixit (2011), Badreddine et al. (2016) and Zhang et al. (2021)). The advantages of this class of thermodynamically-consistent models are that they can easily account for initial and induced anisotropies, cyclic effects, mixed hardening, through the use of advanced yield functions and plastic potentials. However, due to the intrinsic phenomenological nature of this approach, it is not guaranteed that the calibration of a set of parameters for a given loading path would lead to accurate predictions for other types of loading, since the damage parameter is not based on a physical mechanism. On the other hand, several works have made use of micromechanical Gurson-type models to predict failure during sheet metal forming (Uthaisangsuk et al., 2008; Kami et al., 2015; Ying et al., 2018; Bong et al., 2021). Overall, this class of models provides good predictions when the triaxiality is high since in that case damage is mainly driven by void growth. However Gurson's model underestimates damage occurrence in presence of shear, and in that case it requires refinements to account for damage in shear, such as the incorporation of 'shear damage' as done by Ying et al. (2018) in the simulation of punch tests, using Nahshon and Hutchinson (2008)'s phenomenological modification of Gurson's model. However, Nahshon and Hutchinson (2008)'s model predicts an increase of the porosity in pure shear which is in contradiction with micromechanical cell calculations (Morin et al., 2016). Therefore, the accurate simulation of sheet metal forming using a micromechanical model which incorporates void growth and shear effects remains a challenge.

An alternative approach for the simulation of damage under complex strain paths during sheet metal forming is followed in this work. It is based on a micromechanical description of the effect of *void growth* together with *void rotation and elongation*. Indeed, it has been shown recently that ductile failure under shear-dominated loadings is essentially due to important changes of the shape of the voids (Nielsen et al., 2012; Morin et al., 2016). The Madou–Leblond model of plastic porous solids incorporating void shape effects (Madou and Leblond, 2012a,b, 2013; Madou et al., 2013), in which the voids' semi-axes and orientation can evolve, is considered to simulate shear-dominated failure involved in forming processes. It has permitted to reproduce micromechanical cell calculations in shear-dominated loadings as well as experiments on butterfly specimens with shear (Morin et al., 2016, 2017a) using a heuristic coalescence modeling. A specific mention has to be made to the work of Torki and Benzerga (2018), who considered a Gurson-type model together with a micromechanical model of coalescence for spheroidal voids. They succeeded in simulating the complete loss of stress carrying in a material point in shear (due to void shape changes) with a parameter-free model accounting for void rotation and void shape change. However, their work is limited to spheroidal void shapes which can be in general unrealistic for arbitrary (multi-axial) loading states. Therefore, the aim of this paper is to investigate the predictions of the Madou–Leblond model for general ellipsoidal voids in several sheet forming processes in which important shear effects are observed. We will focus on the macroscopic features of failure in the simulation of the following experiments:

- We consider the results of the deep drawing experiments performed by Gorji and Mohr (2018) on aluminum alloy 6016-T4. Those experiments are interesting because two different modes of failure has been observed experimentally, according to the blank size. For large blanks, a (standard) bottom crack is observed while for small blanks, a shear crack is observed.
- We perform new experiments of corrugation processing on aluminum alloy 7075-T6 following the experimental set-up of Ezequiel et al. (2020) (see also Elizalde et al. (2020)). When repeated, this process belongs to severe plastic deformation processing and thus it is meant to induce important shear deformation to achieve grain refinement. Therefore it is a good candidate to investigate damage in shear.

The paper is organized as follows. In Section 2, the experimental procedures on deep drawing and corrugation processing are presented. Section 3 recapitulates the Madou–Leblond model for ductile materials with void shape effects and its numerical implementation. The numerical prediction of damage in deep-drawing processing is investigated in Section 4. Finally, in Section 5 we study the evolution of damage in a corrugation processing.

2. Experimental procedures

2.1. Deep drawing

We consider the deep drawing experiments performed by Gorji and Mohr (2018) (see also Gorji et al. (2016b) and Pack et al. (2018)). In these experiments, the material considered is an aluminum alloy 6016-T4 which is a heat treatable Al–Mg–Si alloy widely used in automotive applications due to its good formability and age-hardening capacity. Its chemical composition is given in Table 1 (Thuillier et al., 2012).

The deep drawing experiments have permitted to characterize the out-of-plane shear fracture. The schematic of the experimental set-up is represented in Fig. 1: it is composed of a cylindrical punch with a 75 mm diameter and 5 mm edge radius and a 77 mm diameter die with 3 mm edge radius. The metal blank has a square shape (of size $L \times L$) and a thickness of 1 mm. A double-sided greased blank is drawn at a speed of 1 mm/s until rupture occurs.

Three different behaviors have been observed, depending on the blank's layout and blank holder force:

[1] It must be noted that Gurson's model is also thermodynamically consistent as it belongs to the class of generalized standard materials if the porosity is discretized with a time-explicit scheme (Enakoutsa et al., 2007).

Table 1
Chemical composition of the Al-6016-T4 alloy.

Element	Mg	Si	Ti	Fe	Cr	Others (Cu, Zn)	Al
wt%	0.25–0.6	1.0–1.5	max 0.15	max 0.5	max 0.1	max 0.2	Balance

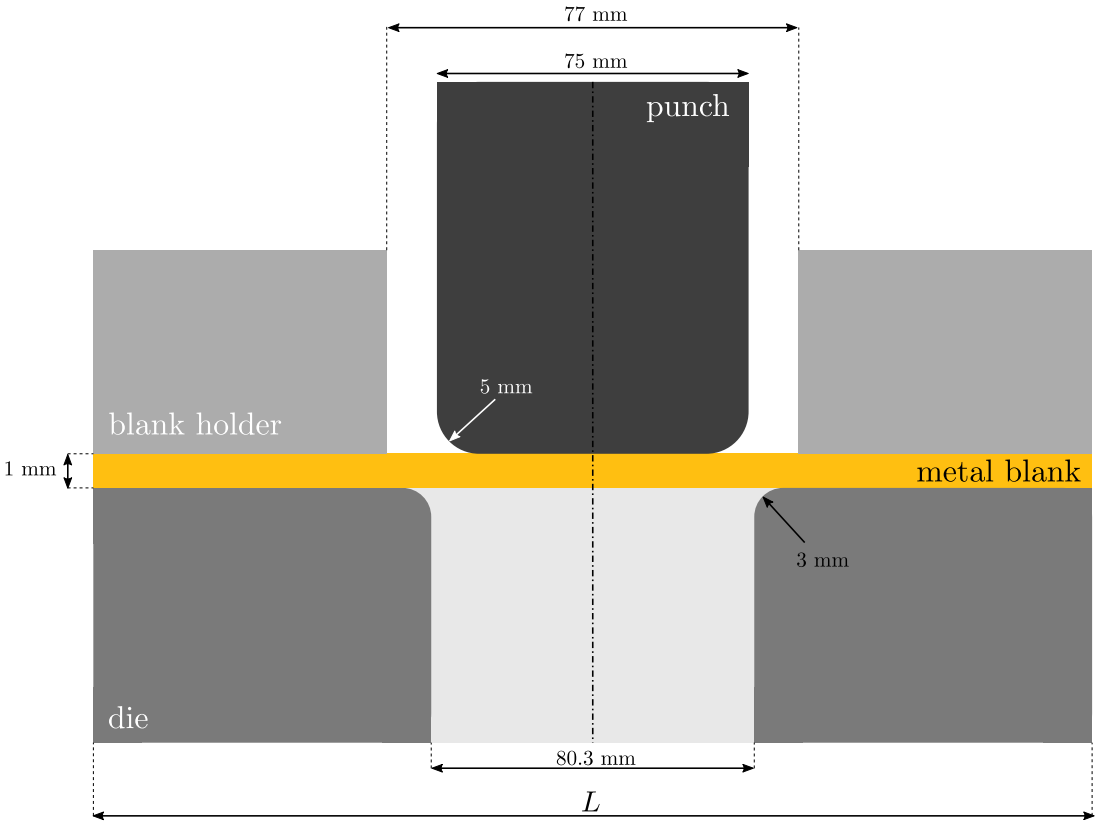

Fig. 1. Set-up of the deep drawing experiments.

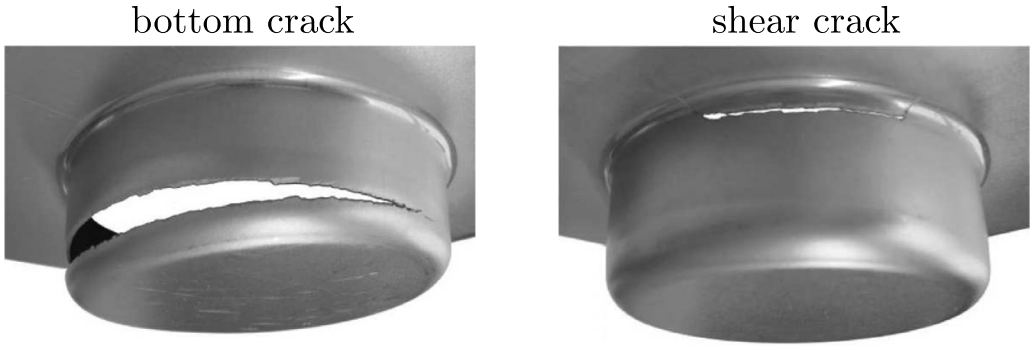

Fig. 2. Location of cracks observed experimentally in deep drawing experiments (after Gorji et al., 2016b). In the case of a blank-holder force of 200 kN, a shear crack appears for a blank size L between 133 mm and 150 mm while a bottom crack occurs for a blank size L above 150 mm.

- *No failure*, which happens for small layouts.
- *Bottom crack*, which is the most typical type of failure in practice. A crack occurs on the side wall, near the punch-side of the workpiece (see Fig. 2).
- *Shear crack*, which may occur at the die profile, when the material is traveling over the corner of the die (see Fig. 2).

It has been observed by Gorji et al. (2016b) that bottom cracks appear for large metal blanks while shear cracks appear for small metal blanks. For a blank-holder force of 200 kN, shear cracks occur for a blank size L between 133 mm and 150 mm while bottom cracks occur for a blank size L above 150 mm. The type of failure is shown in Fig. 3 for various processing conditions. In the case of the shear crack, it has been observed by Gorji et al. (2016b) that the fracture surface is *slanted*. This confirms that this failure mode is due to a shear-dominated loading because slant cracks are generally related to shear band localization (Benzerga and Leblond, 2010).

2.2. Corrugation processing

Experiments of corrugation have been performed on an aluminum alloy 7075-T6 which is widely used in civil aircraft for its excellent characteristics of specific strength and specific stiffness. Its chemical composition is given in Table 2. This Al-7075 alloy was subjected to

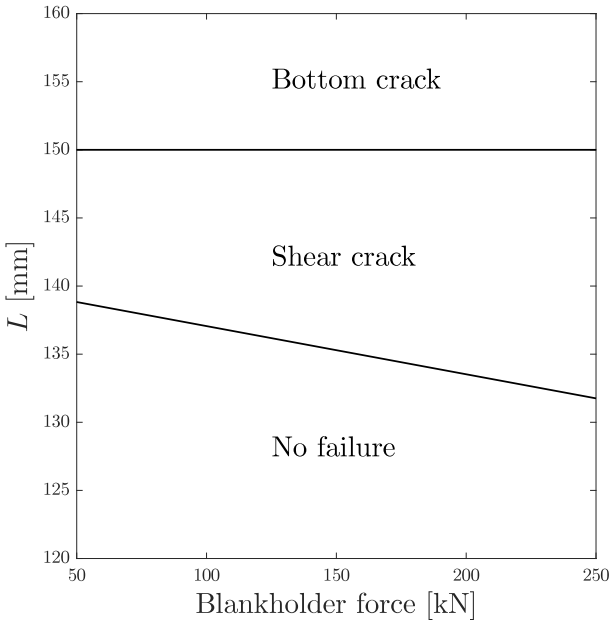

Fig. 3. Type of failure observed during deep drawing depending on the processing conditions (Gorji, 2015).

Table 2
Chemical composition of the Al-7075-T6 alloy.

Element	Si	Fe	Cu	Mn	Mg	Cr	Zn	Ti	Al
wt%	0.23	0.31	1.65	0.22	2.36	0.24	5.72	0.10	Balance

four-stage heat treatment (T6): heating up to 535 °C for 2 h, water tempering, heating up to 175 °C for 18 h, and air cooling down to room temperature.

This corrugation processing considered is the first step of a process called repetitive corrugation and straightening (RCS) which consists of two steps:

(1) An initial flat sheet is corrugated using two corrugation dies, which induce important shear deformation within the sheet. At the end of this step, the specimen is no longer a sheet as its shape is corrugated (see Fig. 4).
(2) Then, the corrugated specimen is straightened using two flat straightening dies. At the end of this step, the specimen is again a flat sheet.

These two steps correspond to a pass. Since at the end of a pass the specimen is flat, the originality of this process is that it is possible to repeat these passes in order to increase the plastic deformation, which would lead to grain refinement (Ezequiel et al., 2020). Here we have considered a case in which the specimen (made of an Al-7075-T6 alloy) fails during the corrugation step of the *first pass*. This case will be useful to study the ability of the model to predict ductile failure, as a first step toward the full simulation of multi-pass RCS with accumulating damage from one pass to another. The die profile is based on two perpendicular sinusoidal functions of period 16 mm (see Elizalde et al. (2020)) which is suitable for a sheet thickness of about 1 mm (see Fig. 4), and is composed of 7 × 7 elementary patterns. The size of the sheet is 120 mm × 120 mm × 1 mm. Furthermore, the experiments of corrugation have been performed without any lubrication.

Tensile tests and corrugation process were performed at a deformation speed of 0.5 and 2 mm/min respectively, using an Instron 5500R (10 kN) and an Instron 8802 (25 kN) universal testing machines. In all the specimens processed, a 'cross crack' is observed in the patterns close to the center (see Fig. 5).

3. The Madou–Leblond model for ductile materials

In this section, we briefly recall the main equations defining the Madou–Leblond model along with its extension by Morin et al. (2016). The reader is referred to Madou and Leblond (2012a,b, 2013) and Madou et al. (2013) for a detailed description of all model developments.

3.1. Primitive form of the model

We consider in this work the Madou–Leblond model (which will be denoted by ML hereafter) which is an extension of Gurson's model including void shape effects, permitting to describe the evolution of cavities during shear-dominated loading supposedly responsible for shear damage. In this model, the elementary cell Ω is ellipsoidal and contains a confocal ellipsoidal cavity ω of semi-axes $a > b > c$ oriented along the (local) unit vectors $\mathbf{e}_x$, $\mathbf{e}_y$, $\mathbf{e}_z$. The cavity surface is characterized by the quadratic form $\mathcal{P}$ defined by

$$\mathcal{P}(\mathbf{u}) \equiv \frac{(\mathbf{u}.\mathbf{e}_x)^2}{a^2} + \frac{(\mathbf{u}.\mathbf{e}_y)^2}{b^2} + \frac{(\mathbf{u}.\mathbf{e}_z)^2}{c^2}. \tag{1}$$

The matrix $\mathbf{P} \equiv (P_{ij})$ of the quadratic form $\mathcal{P}$ is expressed in the fixed frame $(\mathbf{e}_1, \mathbf{e}_2, \mathbf{e}_3)$ of the observer and permits to describe the orientation and semi-axes ratios of the ellipsoidal cavity; indeed its diagonalization provides the semi-axes and the local unit vectors $\mathbf{e}_x$, $\mathbf{e}_y$, $\mathbf{e}_z$ defining the orientation. Another important parameter in this model is the porosity f which is defined as

$$f = \frac{\mathrm{vol}(\omega)}{\mathrm{vol}(\Omega)}. \tag{2}$$

The matrix is supposed to be rigid-perfectly plastic and obeys a von Mises criterion with a yield stress σ_0. A mixed analytical–numerical limit-analysis has been performed on this elementary ellipsoidal cell and led to the macroscopic yield criterion

$$\Phi(\boldsymbol{\sigma}, \mathbf{P}, f, \sigma_0) = \frac{Q(\boldsymbol{\sigma})}{\sigma_0^2} + 2(1+g)(f+g)\cosh\left[\frac{\mathcal{L}(\boldsymbol{\sigma})}{\sigma_0}\right] - (1+g)^2 - (f+g)^2 \leq 0. \tag{3}$$

In Eq. (3):

- $Q(\boldsymbol{\sigma})$ is a quadratic form of the components of the Cauchy stress tensor $\boldsymbol{\sigma}$ defined by

$$Q(\boldsymbol{\sigma}) = \boldsymbol{\sigma} : \mathbb{Q} : \boldsymbol{\sigma} \tag{4}$$

  where $\mathbb{Q}(\mathbf{P}, f)$ is a fourth-order tensor which is related to classical Willis's bound for non-linear composites (see Madou and Leblond (2012b));
- $\mathcal{L}(\boldsymbol{\sigma})$ is a linear form of the diagonal components of $\boldsymbol{\sigma}$ in the basis $(\mathbf{e}_x, \mathbf{e}_y, \mathbf{e}_z)$ defined by

$$\mathcal{L}(\boldsymbol{\sigma}) = \kappa \mathbf{H} : \boldsymbol{\sigma} \tag{5}$$

  where $\kappa(\mathbf{P}, f)$ is a scalar and $\mathbf{H}(\mathbf{P}, f)$ a second-order tensor of unit trace;
- $g(\mathbf{P}, f)$ is the so-called 'second' porosity. It is related to the volume fraction of a fictitious prolate spheroidal void obtained by rotating the completely flat ellipsoid confocal to the ellipsoidal cavity ω about its major axis. This parameter is null in the case of prolate voids, non-zero in the case of oblate voids, and reduces to the classical 'crack density' of Budiansky in the case of penny-shape cracks. It naturally arises in the limit-analysis procedure of the ellipsoidal void and permits to account for the effect of a penny-crack (having a null porosity) on the yield surface (Madou and Leblond, 2012b).

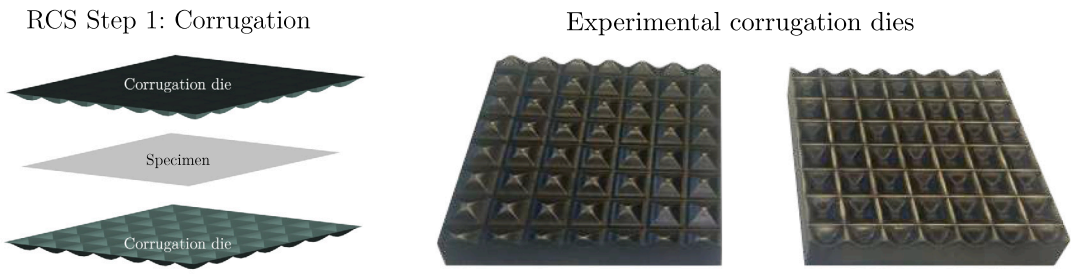

Fig. 4. Set-up of the corrugation experiments.

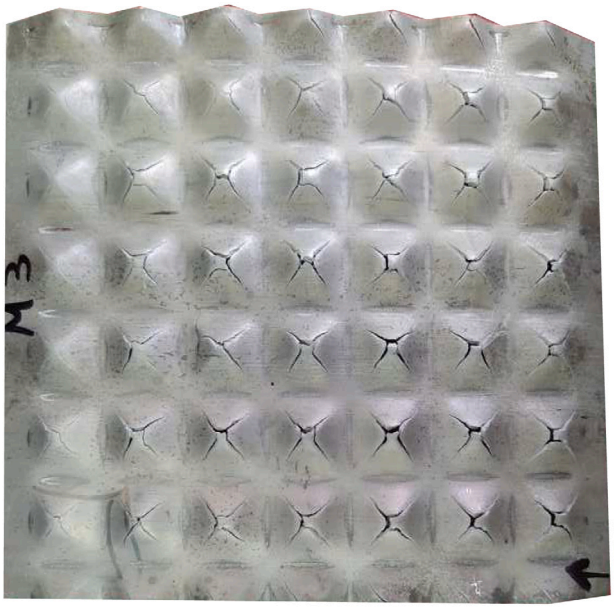

Fig. 5. Location of cracks observed in corrugation experiments.

The details and expressions of all model parameters are given in Madou and Leblond (2012a,b).

The macroscopic yield criterion is then complemented by a macroscopic flow rule which is classically deduced from the normality property (since the normality of the flow rule is preserved during upscaling):

$$\mathbf{D}^p = \dot{\lambda}\left[2\frac{\mathbf{Q}:\boldsymbol{\sigma}}{\sigma_0^2} + \frac{2}{\sigma_0}(1+g)(f+g)\,\kappa\mathbf{H}\sinh\left(\frac{\kappa\mathbf{H}:\boldsymbol{\sigma}}{\sigma_0}\right)\right] \quad ,$$
$$\dot{\lambda}\begin{cases} = 0 & \text{if} \quad \Phi(\boldsymbol{\sigma},\mathbf{P},f,\sigma_0) < 0 \\ \geq 0 & \text{if} \quad \Phi(\boldsymbol{\sigma},\mathbf{P},f,\sigma_0) = 0 \end{cases} \tag{6}$$

where $\mathbf{D}^p$ is the Eulerian plastic strain rate and $\dot{\lambda}$ the plastic multiplier.

The evolution equation of the porosity, corresponding to void growth, is deduced from the incompressibility of the matrix

$$\dot{f}_g = (1-f)\mathrm{tr}(\mathbf{D}^p). \tag{7}$$

Finally, the evolution equation of the matrix $\mathbf{P}$ (characterizing the shape and orientation of the ellipsoidal voids) is given by

$$\dot{\mathbf{P}} = -\mathbf{P}.(\mathbf{D}^v + \boldsymbol{\Omega}^v) - (\mathbf{D}^v + \boldsymbol{\Omega}^v)^T.\mathbf{P} \tag{8}$$

where $\mathbf{D}^v$ and $\boldsymbol{\Omega}^v$ are respectively the strain-rate and rotation-rate tensors of the cavity. These rates are given by:

$$\begin{cases} \mathbf{D}^v &= \mathbb{L} : \mathbf{D}^p \\ \boldsymbol{\Omega}^v &= \boldsymbol{\Omega} + \mathbb{R} : \mathbf{D}^p, \end{cases} \tag{9}$$

where $\boldsymbol{\Omega}$ is the rotation-rate tensor of the material (antisymmetric part of the velocity gradient). The tensors $\mathbb{L}(\mathbf{P},f)$ and $\mathbb{R}(\mathbf{P},f)$ are fourth-order 'localization tensors', as the tensor $\mathbb{L}$ relates the (local) void strain-rate $\mathbf{D}^v$ to the macroscopic strain-rate $\mathbf{D}$, and the tensor $\mathbb{R}$ relates the (local) void rotation-rate $\boldsymbol{\Omega}^v$ to the macroscopic rotate-rate $\boldsymbol{\Omega}$. They are based on plastic corrections of the elastic formula provided by Ponte Castañeda and Zaidman (1994) in the elastic case, determined by numerical analyses. The details and expressions of these tensors can be found in Madou et al. (2013).

3.2. Extensions of the model

Following Morin et al. (2016, 2017a), the primitive ML model is completed using several (heuristic) extensions that allow the model to be applicable for practical materials and situations. This includes notably Tvergaard's parameter, coalescence modeling, strain hardening, nucleation and bounds on the semi-axes.

First we introduce the 'Tvergaard parameter' in both the yield criterion (3) and the flow rule (6). This parameter was introduced in order to account for more realistic shapes of the elementary cell (Tvergaard, 1981). In the ML model, this is done by replacing the term $(f+g)$ by $q(f+g)$, where q is a (heuristic) coefficient which is usually slightly larger than unity. Furthermore, it has been shown in Gologanu (1997) that this parameter should depend on the void shape. Thus, following Gologanu (1997) and Morin et al. (2016), this parameter is given by

$$q = (1-k)q^{\mathrm{prol}} + kq^{\mathrm{obl}} \quad , \quad k = \sqrt{\frac{b^2-c^2}{a^2-c^2}} \quad ,$$
$$\begin{cases} q^{\mathrm{prol}} &= 1 + (q^{\mathrm{sph}}-1)\left[\dfrac{2a/c}{1+(a/c)^2}\right]^{3/2} \\ q^{\mathrm{obl}} &= 1 + (q^{\mathrm{sph}}-1)\left[\dfrac{2a/c}{1+(a/c)^2}\right] \end{cases} \tag{10}$$

where q^{sph} is Tvergaard (1981)'s original value of q for spherical voids, and q^{prol} and q^{obl} those of Gologanu (1997) for prolate and oblate voids.

Since ductile tearing is ultimately due to void coalescence, a simple (phenomenological) model of coalescence is considered. We follow Tvergaard and Needleman (1984)'s classical modification of Gurson (1977)'s model, which consists in replacing the porosity f by some larger fictitious one f^*, once some 'critical value' f_c has been reached. Since in the ML model the relevant parameter in the criterion (leading to softening) is no longer f but $f+g$, Tvergaard and Needleman (1984)'s modification will apply to $f+g$:

$$(f+g)^* = \begin{cases} f+g & \text{if} \quad f+g \leq (f+g)_c \\ (f+g)_c + \delta\left[(f+g)-(f+g)_c\right] & \text{if} \quad f+g > (f+g)_c \end{cases} \tag{11}$$

where $(f+g)_c$ and $\delta > 1$ are parameters. This model is heuristic and has permitted to capture the onset of coalescence in the cases of (i) unit-cell calculations in shear (Morin et al., 2016) and (ii) a butterfly specimen subjected to shear-dominated loadings (Morin et al., 2017a).

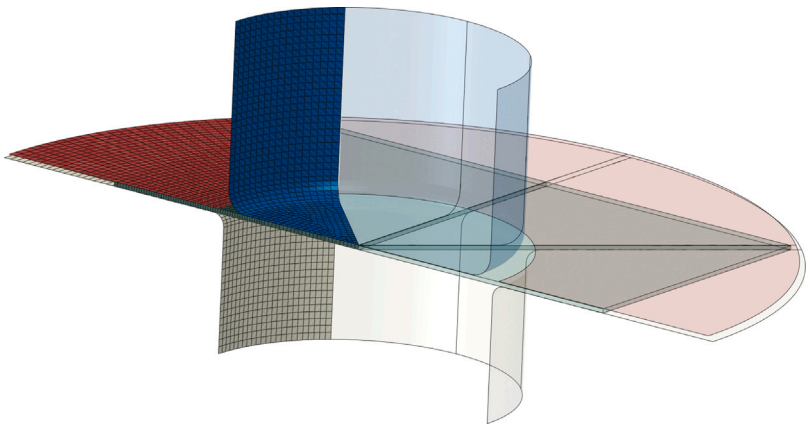

Fig. 6. Mesh considered for the deep drawing simulations. Half of the experimental model is shown as transparent parts and only $1/8^{th}$ of the model is meshed. For illustrative purposes, the distributions of the mechanical quantities will be represented on the whole specimen using symmetry.

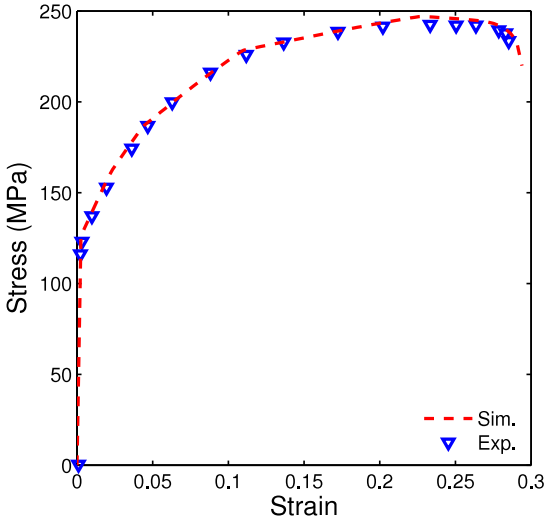

Fig. 7. Experimental and numerical stress–strain curves of the aluminum alloy 6016-T4 used in the deep drawing experiments.

As explained in Section 3.1, the model ML is based on limit-analysis which assumes that the matrix is rigid-perfectly plastic, excluding by essence strain hardening effects. However it can be accounted for approximately by following Gurson (1977)'s approximate approach.[2] The (constant) yield limit σ_0 in the criterion (3) is replaced by some 'average yield stress' $\bar{\sigma}$ given by:

$$\bar{\sigma} \equiv \sigma(\bar{\varepsilon}) \tag{12}$$

where $\sigma(\varepsilon)$ is the function providing the yield limit as a function of the local accumulated plastic strain ε, and $\bar{\varepsilon}$ represents some 'average equivalent strain' in the sound matrix. The evolution of $\bar{\varepsilon}$ is then deduced by assuming that the plastic dissipation on the ML model

$$\boldsymbol{\sigma} : \mathbf{D}^p \tag{13}$$

is equal to the plastic dissipation in some fictitious porous 'equivalent' material which has the same porosity f. In this equivalent material, the plastic dissipation is thus taken as

$$(1-f)\bar{\sigma}\dot{\bar{\varepsilon}}. \tag{14}$$

[2] It could also be possible to use Morin et al. (2017b)'s explicit approach based on sequential limit-analysis.

The evolution equation of $\bar{\varepsilon}$ is then given by

$$\dot{\bar{\varepsilon}} = \frac{\boldsymbol{\sigma} : \mathbf{D}^p}{(1-f)\bar{\sigma}}. \tag{15}$$

Finally, void nucleation is accounted for by considering the strain-controlled model of Chu and Needleman (1980). The nucleation rate is given by

$$\dot{f}_{\mathrm{n}} = \frac{f_N}{s_N\sqrt{2\pi}} \exp\left[-\frac{1}{2}\left(\frac{\bar{\varepsilon}-\varepsilon_N}{s_N}\right)^2\right] \times \dot{\bar{\varepsilon}} \tag{16}$$

where f_N, ε_N and s_N are respectively the volume fraction, average nucleation strain and standard deviation. The evolution equation of the porosity thus reads

$$\dot{f} = \dot{f}_{\mathrm{g}} + \dot{f}_{\mathrm{n}}. \tag{17}$$

In order to unravel the effect each damage mechanisms upon the failure, we will also consider as post-treatments, the 'nucleated porosity' f_{n} and the 'void growth porosity' f_{g} which are defined from their respective rates (16) and (7) by

$$f_{\mathrm{n}} = \int_0^t \dot{f}_{\mathrm{n}}(\tau)\mathrm{d}\tau; \quad f_{\mathrm{g}} = \int_0^t \dot{f}_{\mathrm{g}}(\tau)\mathrm{d}\tau = f - f_{\mathrm{n}} - f_0. \tag{18}$$

It is interesting to note that in the case of void collapse (if $\mathbf{D}^p < 0$), the so-called 'void growth porosity' f_{g} can be negative but it must verify

$$f_{\mathrm{g}} \geq -f_0 - f_{\mathrm{n}} \tag{19}$$

since the total porosity f cannot be negative.

3.3. Scalar damage parameter characterizing failure

In the model ML, softening is due to both the porosity and void shape effects (through the second porosity). Following Morin et al. (2016), it is interesting to define (as a post-treatment) a damage parameter d, tied to both f and g, which characterizes the progressive degradation of the material.

If we assume that the material is entirely failed ($\boldsymbol{\sigma} = \mathbf{0}$), we can obtain from the yield criterion (3):

$$2q(1+g)(f+g)^* - (1+g)^2 - q^2(f+g)^{*2} = -\left(1+g-q(f+g)^*\right)^2 = 0. \tag{20}$$

It follows that $q(f+g)^* = 1+g$. The damage parameter d can thus be defined by

$$d = \frac{q(f+g)^*}{1+g}, \tag{21}$$

the values $d = 0$ and $d = 1$ corresponding to absence of damage and total damage, respectively. This parameter, which does not play any role in the constitutive equations, permits the evaluation, as a post-treatment of the results, of the location and importance of damage in a structure.

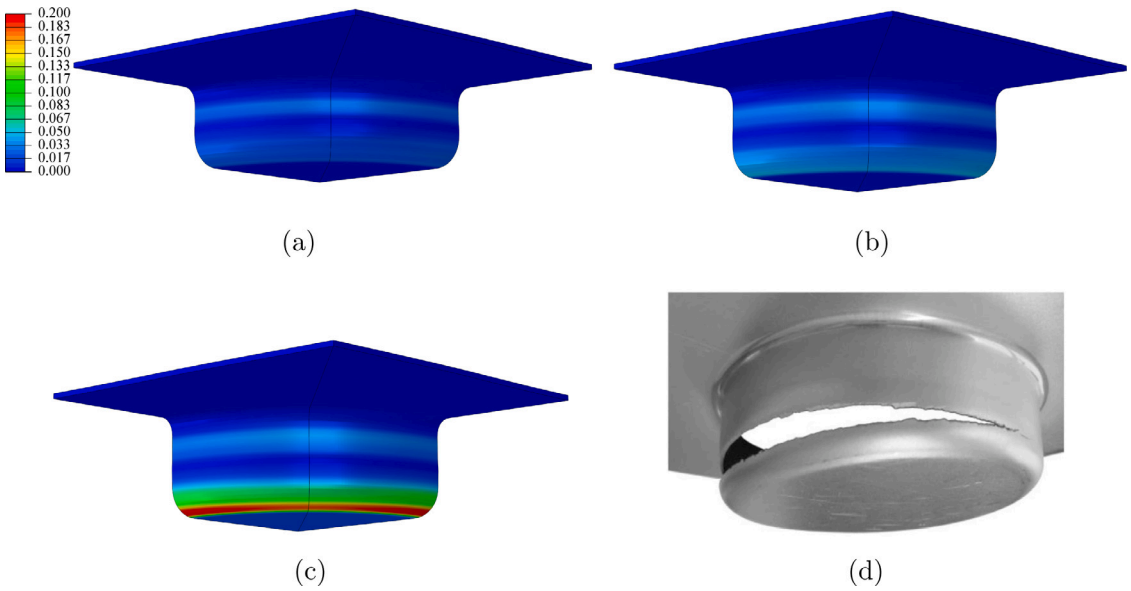

Fig. 8. Location of the bottom crack during deep drawing with a blank size $L = 152$ mm. (a) Distribution of the damage parameter d for a punch displacement of 16 mm, (b) Distribution of the damage parameter d for a punch displacement of 18 mm, (c) Distribution of the damage parameter d for a punch displacement of 20 mm (final step of the simulation) and (d) Photograph of the quasi-fractured specimen (after Gorji and Mohr, 2018).

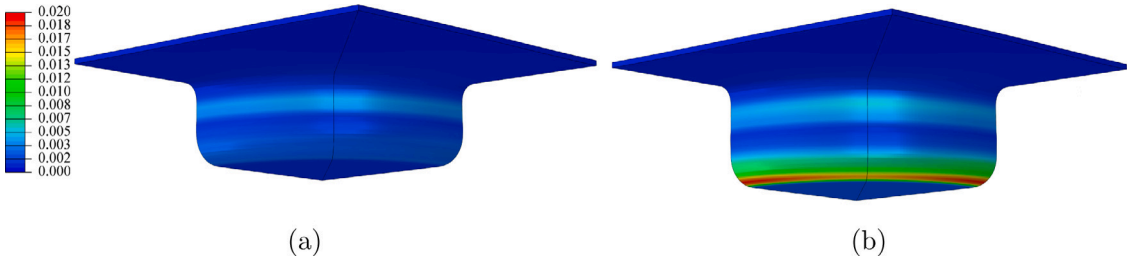

Fig. 9. Distribution of the porosity f in the simulation of a bottom crack during deep drawing with a blank size $L = 152$ mm. (a) Punch displacement of 16 mm and (b) Punch displacement of 20 mm.

3.4. Numerical implementation of the model

The model has been implemented numerically in the finite element code Abaqus through a UMAT procedure (see Morin et al. (2016) and Leblond (2015)). Several ad-hoc modifications have been added to the previous constitutive equations to avoid numerical issues:

- *Contact effects.* Since the ellipsoidal shape can evolve during straining, the semi-axes a, b and c can decrease. In order to avoid negative values after their evolution, contact conditions have been incorporated heuristically. Minimum (positive) values $a_{\min}$, $b_{\min}$ and $c_{\min}$ are prescribed. Then, if at some stage of the calculation the value of a semi-axis, say c, becomes smaller than its minimal value $c_{\min}$, it is replaced by $c_{\min}$. In turns the porosity is adjusted to match the new value (updated) of the semi-axis.
- *Maximal ratio* a/c. As in the previous case, several numerical issues may occur when the ratio a/c is too large, because in that case the matrix $\mathbf{P}$ is ill-defined which leads to numerical problems in the calculation of the eigenvalues. Then, if at some stage of the calculation the ratio a/c becomes larger than a limiting value $(a/c)_{\max}$, it is replaced by $(a/c)_{\max}$. (As before, the porosity is adjusted to match the new value (updated) of the semi-axis).
- *Element deletion.* In practice, softening can become abrupt when the damage parameter reaches high values, typically when $d \geq 0.3$. In absence of void shape effects (i.e. $g = 0$) and using $q = 1.5$, this value would correspond to $f^* = 0.2$ so damage is already very important. Therefore, it is of interest to 'delete' elements that can be considered as (almost) totally damaged. Indeed in practice when such high values are reached, fracture occurs almost instantaneously. Thus, when the damage parameter d becomes larger than a critical value, d_F, the stress is imposed to become nil, that is $\boldsymbol{\sigma} = \mathbf{0}$, which corresponds to element deletion.

3.5. Comments

The ML model contains numerous parameters which in fact depend solely on a small set of initial parameters:

- Initial volume fraction: f_0;
- Initial void shape and orientation of the cavity: $\mathbf{P}_0$;
- Coalescence parameters: $(f+g)_c$ and δ;
- Nucleation parameters: ϵ_N, s_N and f_N.

Once these parameters are known, the yield criterion is fully determined. The porosity f is then evolved using Eq. (17), and the quadratic form is evolved using Eq. (8). If we assume that the voids are initially spherical (which is the case in most practical situations), the matrix $\mathbf{P}_0$ is a multiple of the identify matrix, and the remaining parameters to calibrate (f_0, $(f+g)_c$, δ, ϵ_N, s_N and f_N) correspond to the same parameters that are initially required for GTN model. Therefore, if voids are initially spherical, the calibration of ML can be done exactly as for GTN model, and void shape effects are an *emergent feature* of the model.

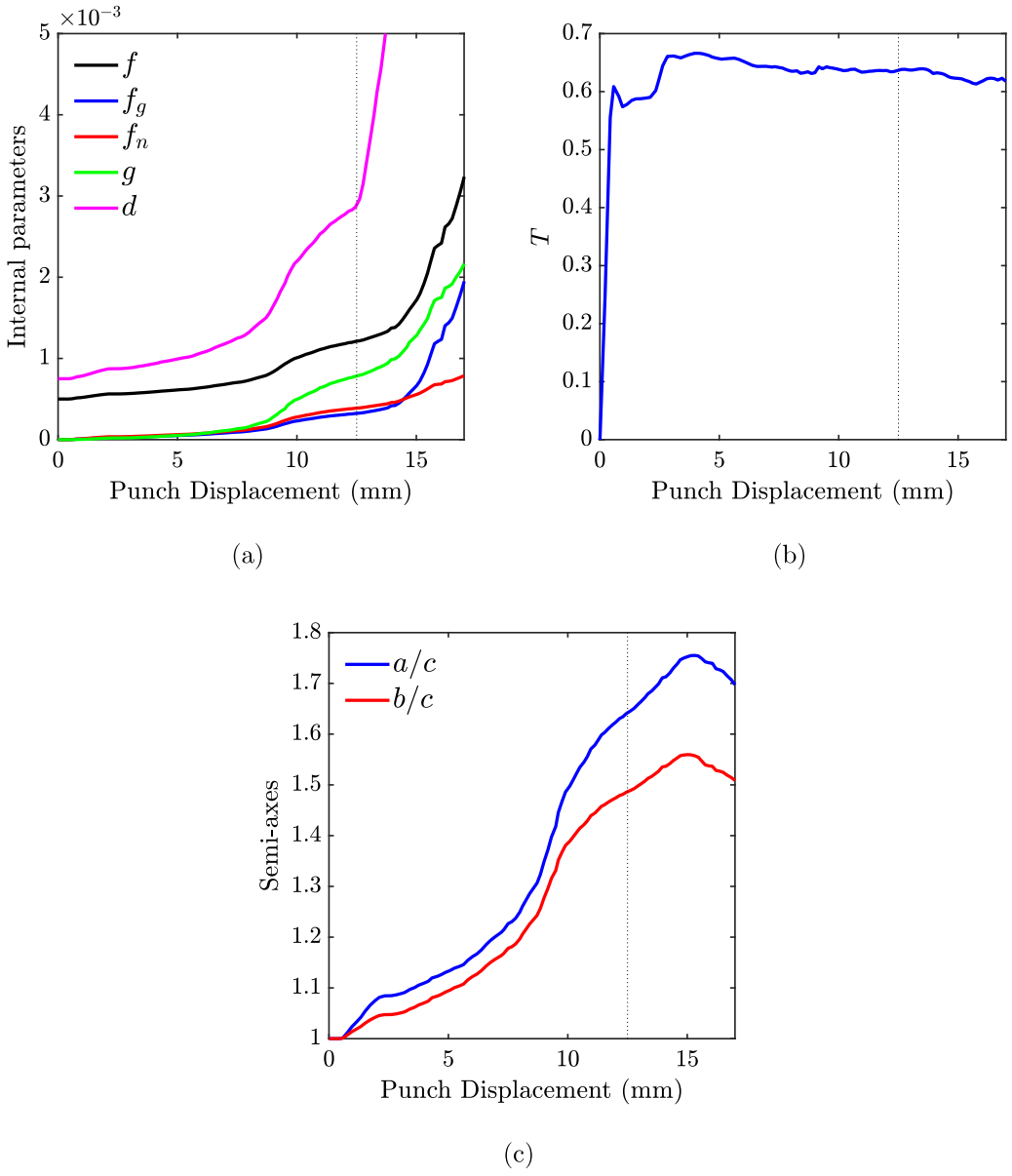

Fig. 10. Evolution of internal parameters in the element that fails first in the simulation of bottom crack during deep drawing (with a blank size $L = 152$ mm). (a) Damage parameter d, total porosity f, second porosity g, nucleated void f_n and porosity due to void growth f_g, (b) Stress triaxiality T and (c) Semi-axes a/c and b/c. The onset of coalescence is represented by a dotted vertical line.

4. Numerical prediction of damage in deep-drawing

4.1. Description of the numerical simulations

Numerical model A 3D finite element model of the deep drawing process has been made using the commercial code ABAQUS/Standard. Due to the symmetry of the process, only $1/8^{th}$ of the specimen is considered (see Fig. 6). The sheet metal is modeled as a 3D deformable part and the mesh is composed of 29 575 elements and 36 276 nodes; we use selectively subintegrated 8-node trilinear brick (C3D8 elements in ABAQUS) which are suitable for quasi-incompressible plasticity as they permit to overcome volumetric locking. The mesh contains 6 elements in the sheet thickness. The punch, blank-holder and die are modeled as rigid 3D shells and are meshed with 2266, 1978 and 2380 R3D4 elements respectively. Contact conditions are considered between the sheet and the rigid parts: the friction is accounted for by a Coulomb friction model in which the frictional force is related to the normal pressure applied on the surface. A value of 0.015 for the friction coefficient was used in the simulations as the blank during the experimental process was completely greased on both sides.

Material parameters An important task concerns the calibration of the ML model parameters for the 6016-T4 aluminum alloy used in the experiments of Gorji and Mohr (2018).

First, since 6016-T4 aluminum alloy exhibits a very small anisotropy (Gorji et al., 2016a; Pack et al., 2018; Cai et al., 2020), we assume that its behavior is isotropic and the hardening behavior of the material is assumed to follow a Swift–Voce law:

$$\sigma(\varepsilon) = \omega A \left(\bar{\varepsilon}_p + \varepsilon_0\right)^n + (1-\omega)\left(k_0 + Q\left(1 - e^{-\beta\bar{\varepsilon}_p}\right)\right), \tag{22}$$

where the parameters ω, A, n, ε_0, k_0, Q and β have been calibrated by Gorji and Mohr (2018) and are provided in Table 3. In Eq. (22), $\bar{\varepsilon}_p$ is the accumulated plastic strain.

The most difficult part concerns the calibration of the parameters related to damage (initial porosity, initial shape of voids, nucleation parameters and coalescence parameters). For the same aluminum alloy AA6016-T4, the initial porosity and nucleation parameters have been

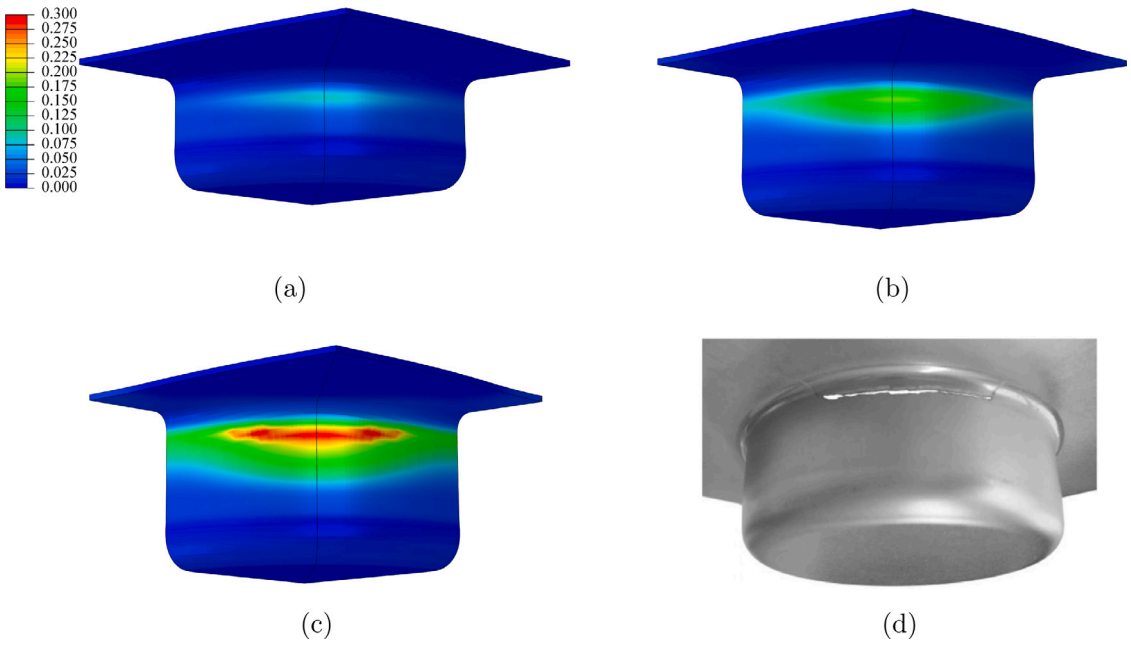

Fig. 11. Location of the shear crack during deep drawing with a blank size $L = 140$ mm. (a) Distribution of the damage parameter d for a punch displacement of 20 mm, (b) Distribution of the damage parameter d for a punch displacement of 25 mm, (c) Distribution of the damage parameter d for a punch displacement of 28.8 mm (final step of the simulation) and (d) Photograph of the quasi-fractured specimen (after Gorji and Mohr, 2018).

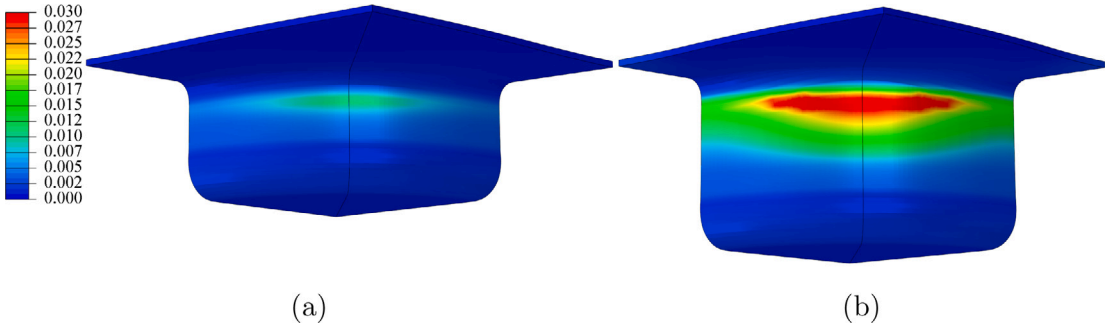

Fig. 12. Distribution of the porosity f in the simulation of a shear crack during deep drawing with a blank size $L = 140$ mm. (a) Punch displacement of 20 mm and (b) Punch displacement of 28.8 mm.

Table 3
Swift–Voce hardening law parameters for the AA6016-T4.

Material	ω	A [MPa]	n	ε_0	k_0 [MPa]	Q [MPa]	β
AA6016-T4	0.739	286.15	0.229	0.0161	160.1	464.5	9.89

Table 4
Parameters for the model ML in the case of the AA6016-T4.

	q	f_0	$(f+g)_c$	δ	f_N	ε_N	s_N	d_F	$(P_0)_{ij}$
AA6016	1.5	0.0005	0.002	6	0.018	0.9	0.4	0.3	δ_{ij}

calibrated by Thuillier et al. (2012) using X-ray micro-tomography during interrupted tensile tests. In several test samples, the initial volume fraction was found to vary in-between 4.64×10^{-4} and 5.98×10^{-4}; therefore we have considered the value $f_0 = 5 \times 10^{-4}$. Furthermore, in the initial state, voids can be considered as spherical so that the initial matrix $\mathbf{P}_0$ is a multiple of the identity matrix; we thus consider that $(P_0)_{ij} = \delta_{ij}$ (where δ_{ij} is Kronecker symbol). A value $q = 1.5$ was classically considered for the Tvergaard parameter. Then, the experimental evolution of the void volume fraction as a function of the strain (in a tensile test) has permitted to calibrate the nucleation parameters (see Thuillier et al. (2012)): $f_N = 0.018$, $\varepsilon_N = 0.9$ and $s_N = 0.4$. The coalescence parameters are calibrated by fitting the model's predictions with the evolution of void volume fraction provided by Thuillier et al. (2012): this leads to $(f + g)_c = 0.002$ and $\delta = 6$. Finally, a value $d_F = 0.3$ was chosen for the element deletion (in order to avoid numerical instabilities during total fracture). A summary of all the damage parameters is given in Table 4.

It must be noted that the critical value $(f + g)_c$ that has been calibrated *seems* small, although it is in the range of actual values from the literature for GTN model (Benseddiq and Imad, 2008). Furthermore, it has been shown by Springmann and Kuna (2005) that, in the case of GTN model, several sets of parameters (f_0, f_c) can lead to nearly similar predictions of a tensile test. They notably show that an increase of f_0 of one order of magnitude requires that f_c is also increased by one order of magnitude. Therefore, since we considered a very small value for the initial porosity $f_0 = 5 \times 10^{-4}$, it is not surprising that the critical value is 'small'. Nonetheless, the ratio $(f + g)_c/f_0$ (which is equal to 4) and the value of δ are in agreement with previous numerical studies of shear-dominated fracture using the model ML (Morin et al., 2016, 2017a).

The experimental stress–strain curve of the aluminum alloy 6016-T4 is compared to the predictions of the model (using the calibrated

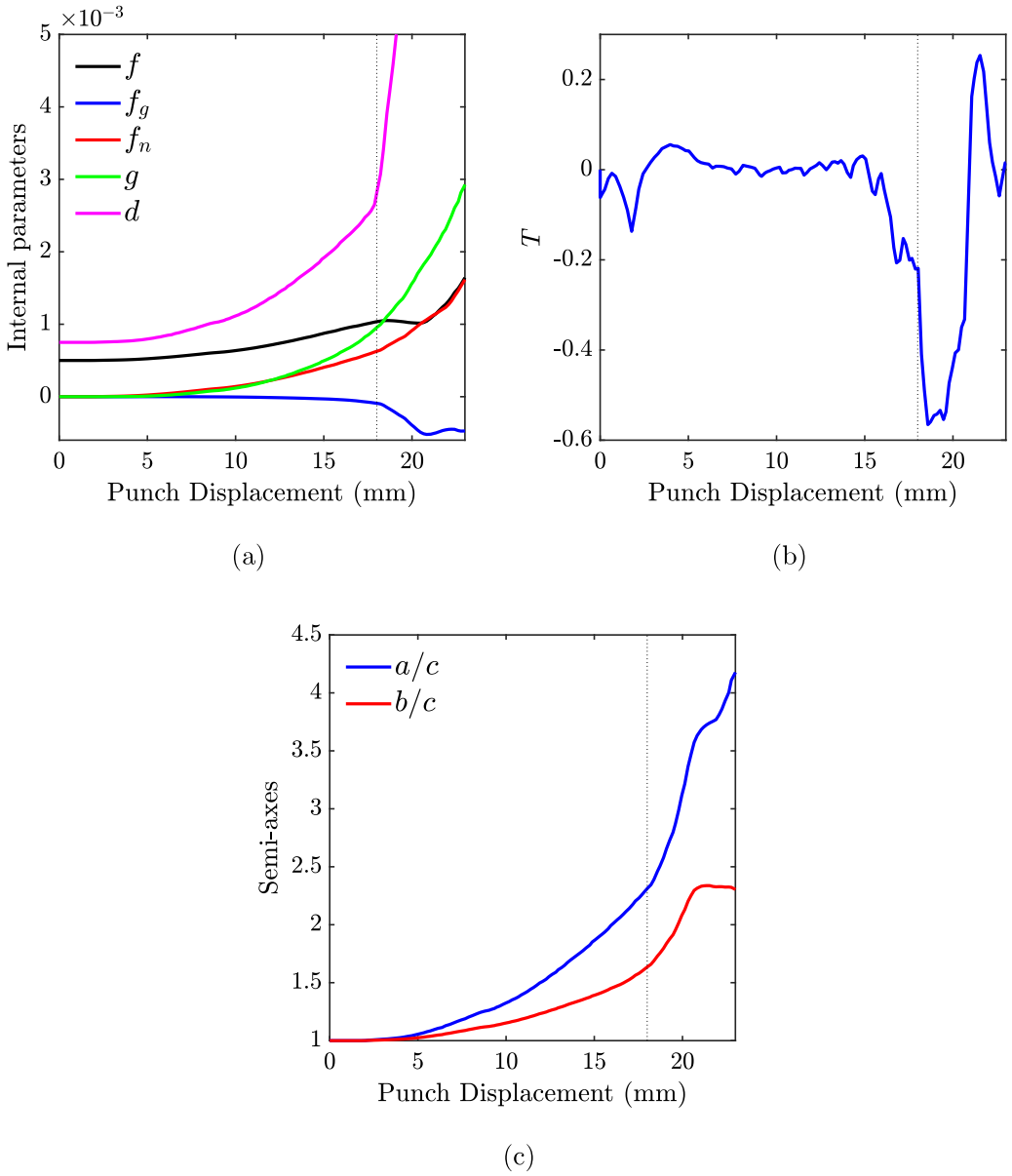

Fig. 13. Evolution of internal parameters in the element that fails first in the simulation of a shear crack during deep drawing with a blank size $L = 140$ mm. (a) Damage parameter d, total porosity f, second porosity g, porosity due to nucleation f_n and porosity due to void growth f_g, (b) Stress triaxiality T and (c) Semi-axes a/c and b/c. The onset of coalescence is represented by a dotted vertical line.

parameters) in Fig. 7. Overall, a good agreement is observed between the numerical and experimental stress–strain curves.

Process conditions The deep-drawing process will be considered for a blank-holder force $F = 200$ kN. For this force, it was observed experimentally that the cracking mode depends on the blank size. Hence, several blank sizes, ranging from 130 mm to 152 mm, will be considered in the numerical simulations to study the cracking mode. We will then present detailed results in only two cases which lead to different damage mechanisms. We consider (i) a large blank size $L = 152$ mm for which a *bottom crack* occurs and (ii) a small blank size $L = 140$ mm, for which a *shear crack* occurs.

Quantities investigated Several quantities will be studied in order to investigate the damage occurrence during deep drawing: (i) the distribution of the damage parameter d and the porosity f in the whole specimen at several snapshots and (ii) the evolution of several internal parameters (f, f_n, f_g, g, d, and semi-axes ratios) and the triaxiality (T) in the element that fails first.

4.2. Simulation of a bottom crack

We begin with the simulation of a bottom crack during deep drawing with a blank-holder force $F = 200$ kN. For this force, bottom cracks are simulated numerically for blank sizes roughly higher than 145 mm, which is in agreement with the experimental observations (see Fig. 3).

In the case $L = 152$ mm which is considered hereafter, the numerical simulation ends at a displacement of about 20 mm, due to a numerical instability: the very final stage of the fracture process becomes unstable and the final softening is abrupt, the slope of the force–displacement curve becoming vertical. Hence, the bottom crack simulated numerically occurs for a punch displacement which is in agreement with the experimental value (of about 20.5 mm).

The distribution of the damage parameter d is represented for several punch displacements (16 mm, 18 mm and 20 mm which corresponds to final step of the calculation) and is compared to the fractured specimen in Fig. 8. It is slightly asymmetric due to the presence of corners in the sheet. The location of the crack at the bottom of the

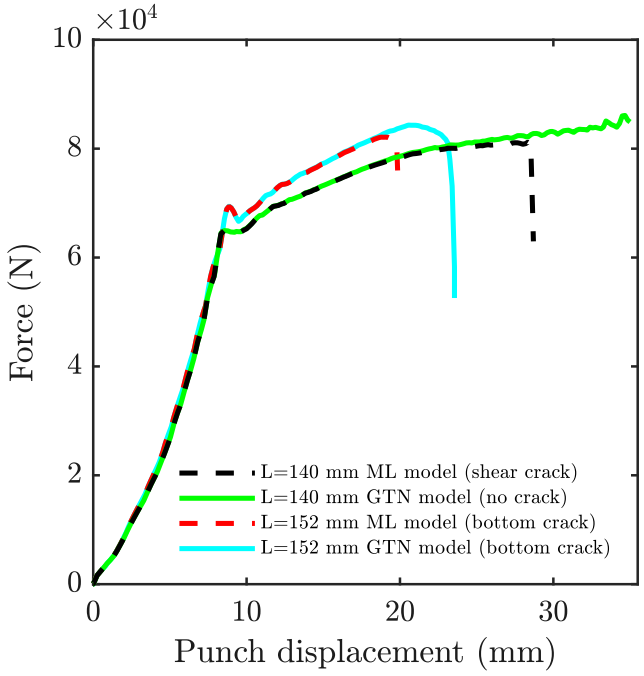

Fig. 14. Comparison of the punch force–displacement curves using ML and GTN for the two blank sizes considered ($L = 140$ mm and $L = 152$ mm).

specimen (through the damage parameter d) is globally well reproduced by the ML model during the simulation, by comparison to the photograph of the quasi-fractured specimen (Fig. 8). The crack location is slightly more toward the base than in the experimental results, which can be due to the value considered for the friction coefficient. Indeed, a modification of the friction coefficient can cause necking and fracture to initiate at different locations without modifying much the overall behavior (see e.g. Zhang et al. (2017)).

In addition, the distribution of the porosity f is represented in Fig. 9 for two punch displacements (16 mm and 20 mm). The distribution of the porosity is very similar to that of the damage parameter in terms of pattern. However, the maximal value of the porosity reaches 0.02 while it was roughly 0.2 for the damage parameter (for a punch displacements of 20 mm). Therefore, according to the definition of the damage parameter d (see Eq. (21)), the difference between the values of d and f can be attributed by two factors, void shape effects (through the second porosity g) and/or coalescence (through the term $(f+g)^*$).

In order to investigate the role of each mechanism in the final failure, the evolution of the total porosity f, second porosity g, nucleated porosity f_n (defined by Eq. (18)), void growth porosity f_g (defined by Eq. (18)), stress triaxiality T and semi-axis ratios a/c and b/c are represented (versus the punch displacement) in Fig. 10 in the element that fails first. Prior to the coalescence occurrence (for a punch displacement before 13 mm), it is interesting to note that both f_g, f_n and g increase, with similar rates. Therefore, it can be considered that the onset of coalescence is equitably triggered by void growth, void nucleation and void shape effects. The importance of void growth and nucleation on ductile failure during deep drawing with large blanks is actually expected as it was shown in previous works that Gurson's model (for spherical voids) permits to reproduce the location of bottom cracks (see e.g. Kami et al. (2014)). However, it is still interesting to note that in this case, the triaxiality in this element is roughly constant before localization with a value $T \sim 0.6$: this corresponds to a bi-axial stress state. This is confirmed by the evolution of the semi-axis a/c and b/c, as the major and middle axes are almost the same during the evolution so that the cavity is close to an oblate spheroidal void. The maximal value for the semi-axes ratio is of about $a/c \sim 1.7$ which can be considered as *moderate* void shape effects.

It is important to note that the evolution of the internal parameters is not shown during the entire coalescence stage because the coalescence modeling is heuristic so that after coalescence, the evolution of the internal parameters should be interpreted carefully (Morin et al., 2016). Indeed, once coalescence begins, the quantity $(f+g)$ is replaced by $(f+g)^*$ (using the heuristic model of Tvergaard and Needleman (1984)) in the criterion and the plastic flow rule. Hence, the criterion and plastic flow are modified, which in turns increases (notably) the void growth rate. This explains that the porosity f starts increasing rapidly. Interestingly, the second porosity g also increases rapidly, although void shape effects seem to decrease as the ratios a/c and b/c decrease after a punch displacement of 15 mm.

4.3. Simulation of a shear crack

We continue with the simulation of a shear crack (still with a blank-holder force $F = 200$ kN). For this blank-holder force, shear cracks always occur for a blank size roughly between 130 mm and 145 mm, which is in agreement with the experimental observations (see Fig. 3).

In the case $L = 140$ mm which is considered hereafter, the numerical simulation ends at a displacement of about 28.8 mm, due to a numerical instability: indeed, as in the case of a bottom crack, the very final stage of the fracture process becomes unstable. Therefore, the shear crack simulated numerically occurs for a punch displacement which is in agreement with the experimental value (of about 27.4 mm). In both cases (numerically and experimentally), the punch displacement leading to the shear crack is higher than that leading to the bottom crack.

The distribution of the damage parameter d is represented for several punch displacements (20 mm, 25 mm and 28.8 mm just at the final step) and is compared to a photograph of the quasi-fractured specimen in Fig. 11. As in the case of a bottom crack, the distribution of the damage parameter is asymmetric due to the presence of corners in the sheet. The location of the crack is well reproduced by the ML model during the simulation, by comparison with the photograph of the quasi-fractured specimen. Interestingly this location differs from that usually observed for large blanks (bottom crack). Indeed, in the shear crack case the crack initiates at the top of the sheet instead of the bottom. Furthermore, it is remarkable to note that the initiation of the experimental crack, namely in the region of the sheet corner, is also reproduced by the numerical simulation, emphasizing that the numerical calculation is able to predict the experimental cracking behavior.

As in the case of the bottom crack, the distribution of the porosity, which is represented in Fig. 12 for several punch displacements (20 mm and 28.8 mm), is very similar to that of the damage parameter, but their maximal values are very different (the porosity reaches 0.03 while the damage parameter reaches 0.3). Again, this difference is due to a coupling between void shape effects and coalescence.

The evolution of the total porosity f, second porosity g, nucleated porosity f_n, void growth porosity f_g, triaxiality T and semi-axes ratios a/c and b/c are represented (versus the punch displacement) in Fig. 13 in the element that fails first. Before the coalescence occurrence (i.e. for a punch displacement before 18 mm), it is interesting to note that the 'partial porosity' due to void growth (f_g) decreases while the 'partial porosity' due to nucleation f_n as well as the second porosity g increase, with similar proportions. Therefore, in the case of a shear crack, the model predicts no void growth of initial voids but a small void closure. The increase of the quantity $(f+g)$ is thus solely due to void shape (through g) and void nucleation (through f_n). If void nucleation would have been disregarded, the total porosity f would have decreased; in such case, the threshold $(f+g)_c$ can be attained only with an increase of g which corresponds to void shape effects. Here, in the present case, the threshold $(f+g)_c$ is attained due to an increase of both g and f_n,

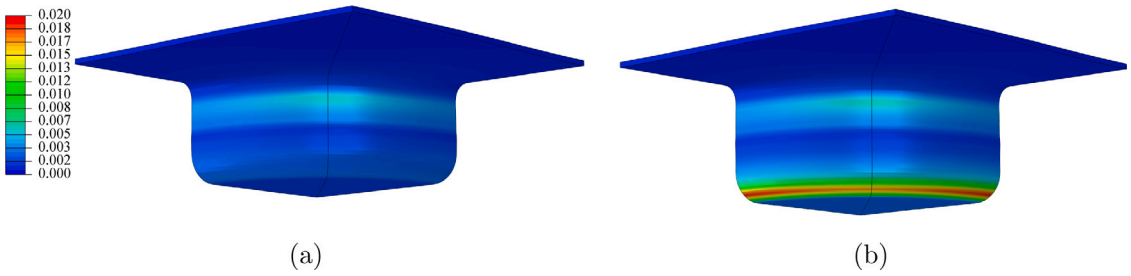

Fig. 15. Distribution of the porosity using the GTN model in the simulation of deep drawing with a blank size $L = 152$ mm. (a) Punch displacement of 20 mm and (b) Punch displacement of 23.7 mm.

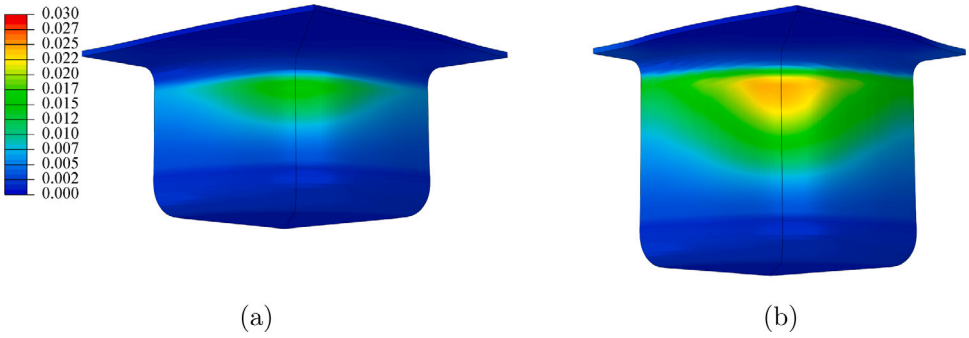

Fig. 16. Distribution of the porosity using the GTN model in the simulation of deep drawing with a blank size $L = 140$ mm. (a) Punch displacement of 28.8 mm and (b) Punch displacement of 35 mm.

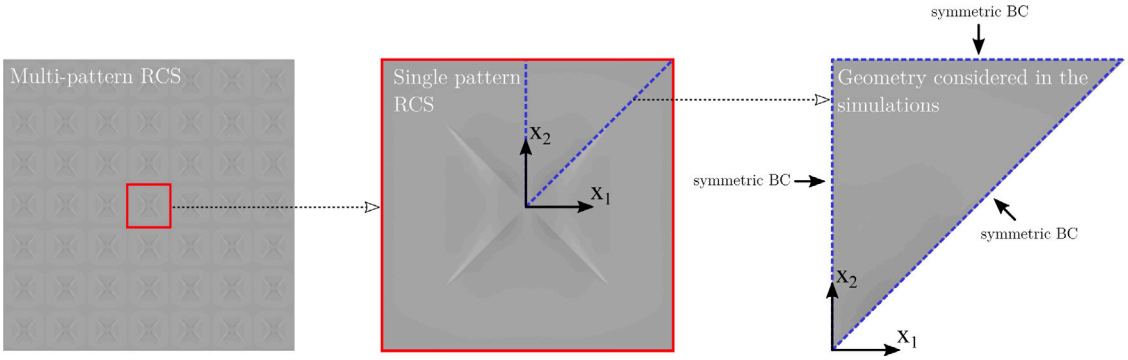

Fig. 17. Geometry considered in the simulations of corrugation.

but the rate of g is higher than the rate of f_n, emphasizing that void shape effects are dominant in this problem and void nucleation plays a minor role. It is worth noting that the stress triaxiality is of about $T \sim 0$ before coalescence, confirming that the local stress state is pure shear (which explains the decrease of the porosity f_g due to the sole void closure mechanism). In that case, important void shape effects are observed, as the void semi-axes ratios reach respectively $a/c \sim 4.25$ and $b/c \sim 2.25$: the cavity has become a general ellipsoidal void with three very different axes $a > b > c$. The predictions of the model are in agreement with the findings of Gorji and Mohr (2018) who postulated that the damage mechanism in that case was due to shearing.

Again, it should be also noted that after coalescence the evolution of the internal parameter should be interpreted even more carefully than in the bottom crack case (Morin et al., 2016). Indeed after coalescence, when the quantity $(f + g)$ is replaced by $(f + g)^*$, artificial void growth can be observed even during pure shear. This is due to the heuristic model of coalescence of Tvergaard and Needleman (1984), as shown previously by Morin et al. (2016).

Table 5
Parameters for the Gurson model in the case of the AA6016-T4.

	q	f_0	f_c	δ	f_N	ε_N	s_N	d_F
AA6016	1.5	0.0005	0.002	4	0.018	0.9	0.4	0.3

4.4. Comparison with Gurson's model

The predictions of the ML model are now compared to that of Gurson's model, in order to assess the importance of void shape effects on shear-dominated ductile fracture.

First, the set of parameters calibrated for the ML model (see Table 4) was found to slightly underestimate ductility during the tensile test. Therefore, an appropriate calibration for Gurson's model parameters has been performed in order to reproduce accurately the tensile test (see Table 5 for the set of parameters).

The force–displacement curves of the punch obtained using Gurson's model are compared to that obtained with the ML model in Fig. 14, for the two cases considered ($L = 140$ mm and $L = 152$ mm). Before the total failure, the overall behavior is quite similar irrespective of the model used.

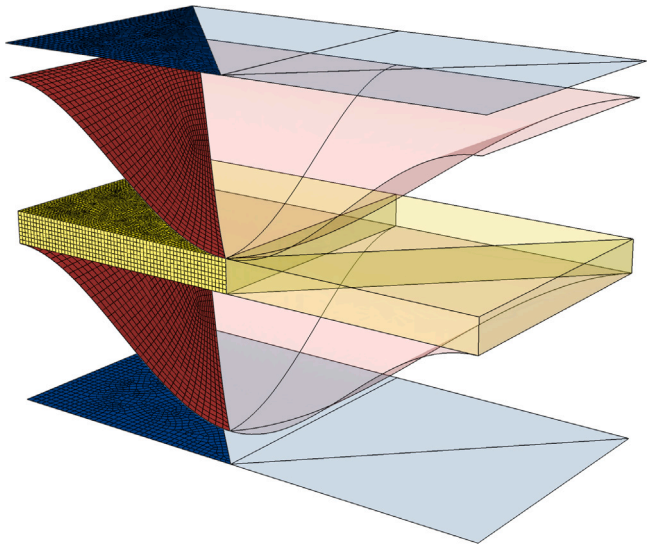

Fig. 18. Mesh considered in the simulations of corrugation. Half of the experimental model is shown as transparent parts and only $1/8^{th}$ of the model is meshed. The sheet is shown in yellow, the corrugation dies in red and the straightening dies in blue.

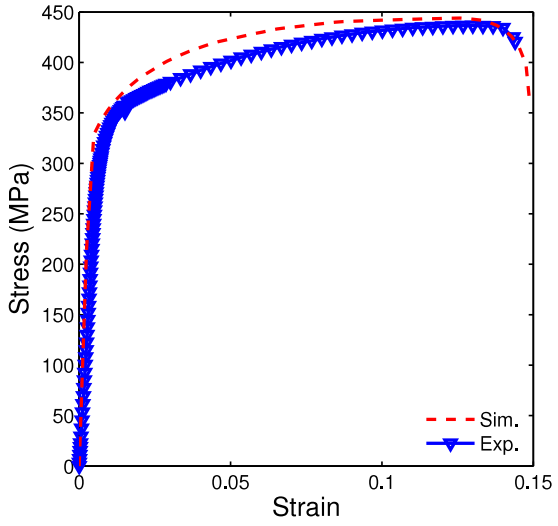

Fig. 19. Experimental and numerical stress–strain curves of the aluminum alloy 7075-T6 used in the corrugation experiments.

In the case of a large blank size ($L = 152$ mm), failure occurs for a displacement of about 23.7 mm using Gurson's model. (Note that failure occurred for a displacement of about 20 mm using the ML model). The distribution of the porosity, for Gurson's model, is represented in Fig. 15. For a punch displacement of 20 mm, the damage parameter is not localized yet at the bottom of the specimen but it localizes for a displacement of 23.7 mm. Therefore, Gurson's model is, as expected, able to predict the bottom crack (as the triaxiality is positive) but it slightly overestimates the ductility as the displacement at failure is higher than that observed experimentally (20.5 mm).

In the case of a small blank size ($L = 140$ mm), there is no failure (at least for the displacements considered) using Gurson's model while failure was predicted using the ML model for a punch displacement of about 28.8 mm. The distribution of the porosity, for Gurson's model, is represented in Fig. 16 for two displacements of the punch (28.8 and 35 mm). Using Gurson's model, the damage parameter is not localized in contrast with the ML model which predicts a localization of damage

Table 6
Swift hardening law parameters for the AA7075-T6.

Material	A [MPa]	n	ε_0
AA7075-T6	673.85	0.1529	0.0075

Table 7
Parameters for the model ML in the case of the AA7075-T6.

	q	f_0	$(f+g)_c$	δ	f_N	ε_N	s_N	d_F	$(P_0)_{ij}$
AA7075	1.5	0.0005	0.005	4	0.01	0.6	0.2	0.3	δ_{ij}

leading to a macroscopic crack. Thus in that case, Gurson's model is not able to predict the shear crack; this was expected as this model does not predict softening in shear because there is no increase of the porosity (which is the damage parameter in this model) in pure shear.

5. Numerical prediction of damage in corrugation processing

5.1. Description of the numerical simulations

Numerical model A 3D finite element model of the corrugation processing has been made using the commercial code ABAQUS/Standard. Following Tajdary et al. (2021) (see also Ezequiel et al. (2020)), the simulation of multi-pattern RCS can be performed on a single elementary pattern subjected to symmetric boundary conditions on its lateral edges (see Fig. 17). Furthermore, due to the symmetry of the process within one pattern, only $1/8^{th}$ of the pattern is meshed and symmetric boundary conditions are applied in the middle of the model; a sketch of the mesh is represented in Fig. 18. The sheet metal is modeled as a 3D deformable part and the mesh is composed of 20 288 elements and 23 823 nodes; as in the deep drawing simulation, we use selectively subintegrated 8-node trilinear brick (C3D8 elements in ABAQUS) which are suitable for quasi-incompressible plasticity. The mesh contains 10 elements in the sheet thickness. The corrugation and straightening dies are modeled as rigid 3D shells and are meshed with 1039 and 958 R3D4 elements respectively. Contact conditions are considered between the sheet and the rigid parts using a Coulomb friction model, with a value of 0.25 for the friction coefficient (see Ezequiel et al. (2020)). In this case the value for the friction coefficient is higher than that considered in the deep drawing problem because the corrugation experiments have been performed without lubrication. It should be noted that, as explained in Section 2, failure occurs during the corrugation step for this material, so the straightening step is not reached in those simulations.

Material parameters Recent experimental works have shown that aluminum alloys 7075 exhibit a moderate anisotropy (Pandya et al., 2020); therefore as a first approximation we assume that its behavior is isotropic and the hardening behavior follows a Swift law:

$$\sigma(\varepsilon) = A(\varepsilon_0 + \bar{\varepsilon})^n \tag{23}$$

where the parameters A and ε_0 have been calibrated using a tensile test (see also Yang et al. (2021) for a similar calibration) and are provided in Table 6.

Then, as in the case of the aluminum alloy AA6016-T4, one needs to calibrate the parameters related to damage. Accordingly, several simulations of the tensile test were performed in order to find the set of parameters that reproduces at best the experimental tensile test. The calibrated set of parameters is given in Table 7. In this case, the ratio $(f+g)_c/f_0$ (equal to 4) and the value of δ are in agreement with the results obtained in Morin et al. (2016).

The experimental stress–strain curve of the aluminum alloy 7075-T6 is compared to the predictions of the model (using the calibrated parameters) in Fig. 19. Overall, a good agreement is observed between the numerical and experimental stress–strain curves.

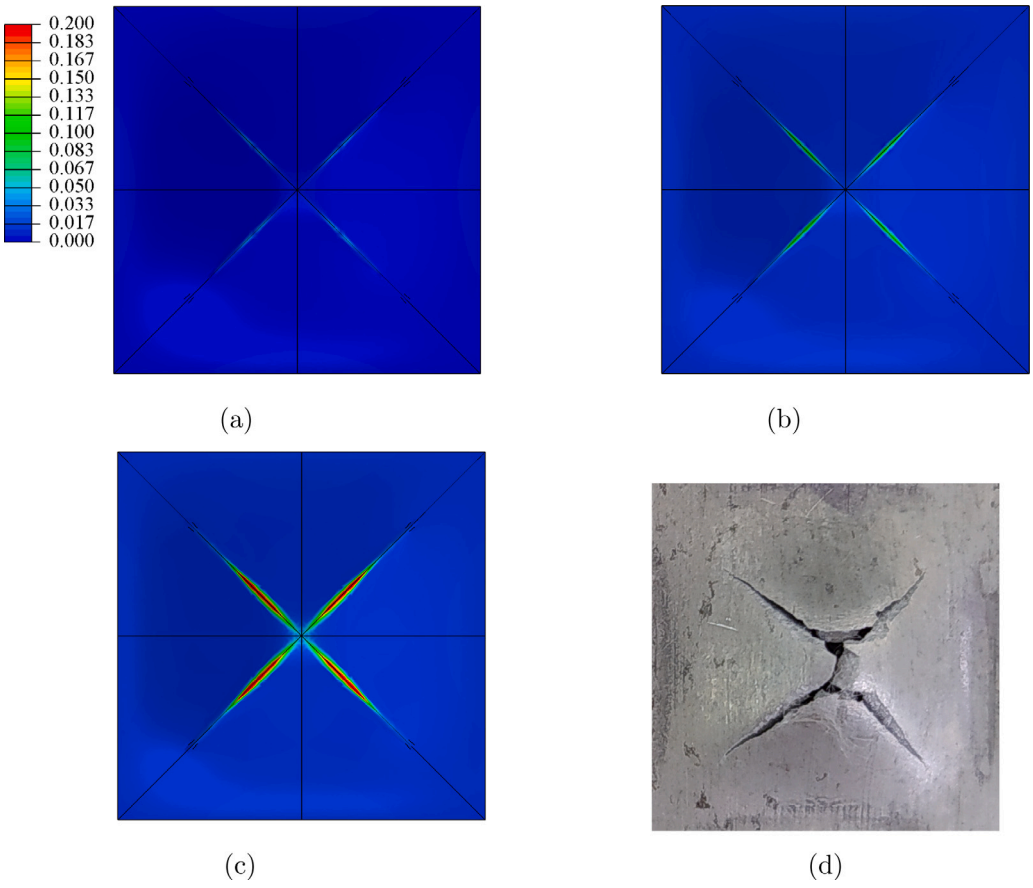

Fig. 20. Location of the 'cross-shaped' crack in the corrugation process. (a) Distribution of the damage parameter d for a die displacement of 2.8 mm, (b) Distribution of the damage parameter d for a die displacement of 3 mm, (c) Distribution of the damage parameter d for a die displacement of 3.3 mm (final step of the simulation) and (d) Photograph of the cross-shaped crack (on one motif) of the quasi-fractured multi-motif specimen (after a displacement of 3.2 mm).

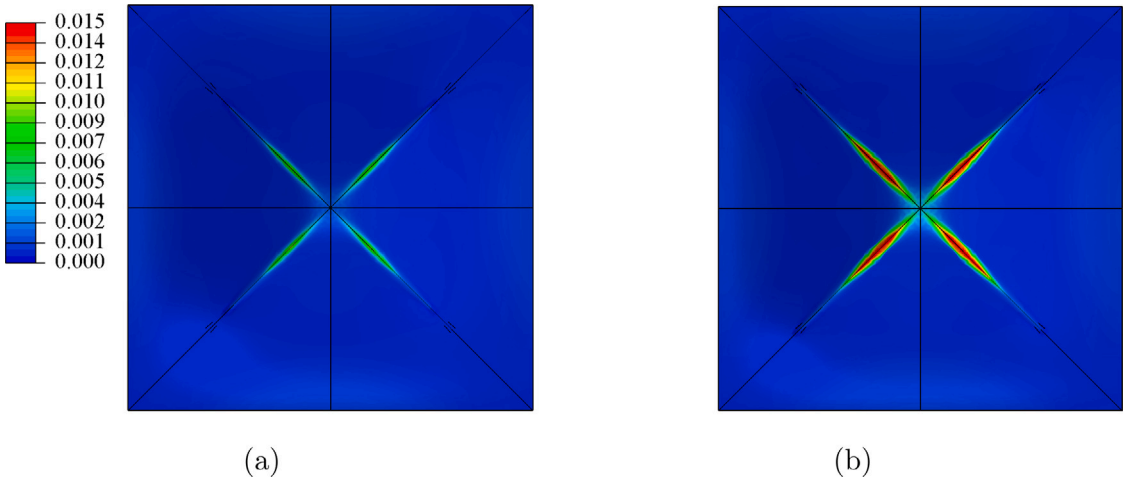

Fig. 21. Distribution of the porosity f in the simulation of corrugation processing. (a) Die displacement of 3 mm and (b) die displacement of 3.3 mm.

Quantities investigated As in the case of deep drawing, several quantities will be studied in order to investigate the damage occurrence: (i) the distribution of the damage parameter d and the porosity f in the whole specimen at several snapshots and (ii) the evolution of several internal parameters (f, f_n, f_g g, d, and semi-axes ratios) and the triaxiality (T) in the element that fails first.

5.2. Results

The numerical simulation ends at a die displacement of about 3.3 mm, due to a numerical instability (the slope of the force–displacement curve becomes vertical). The crack simulated numerically thus occurs for a die displacement which is in agreement with the experimental value (of about 3.2 mm).

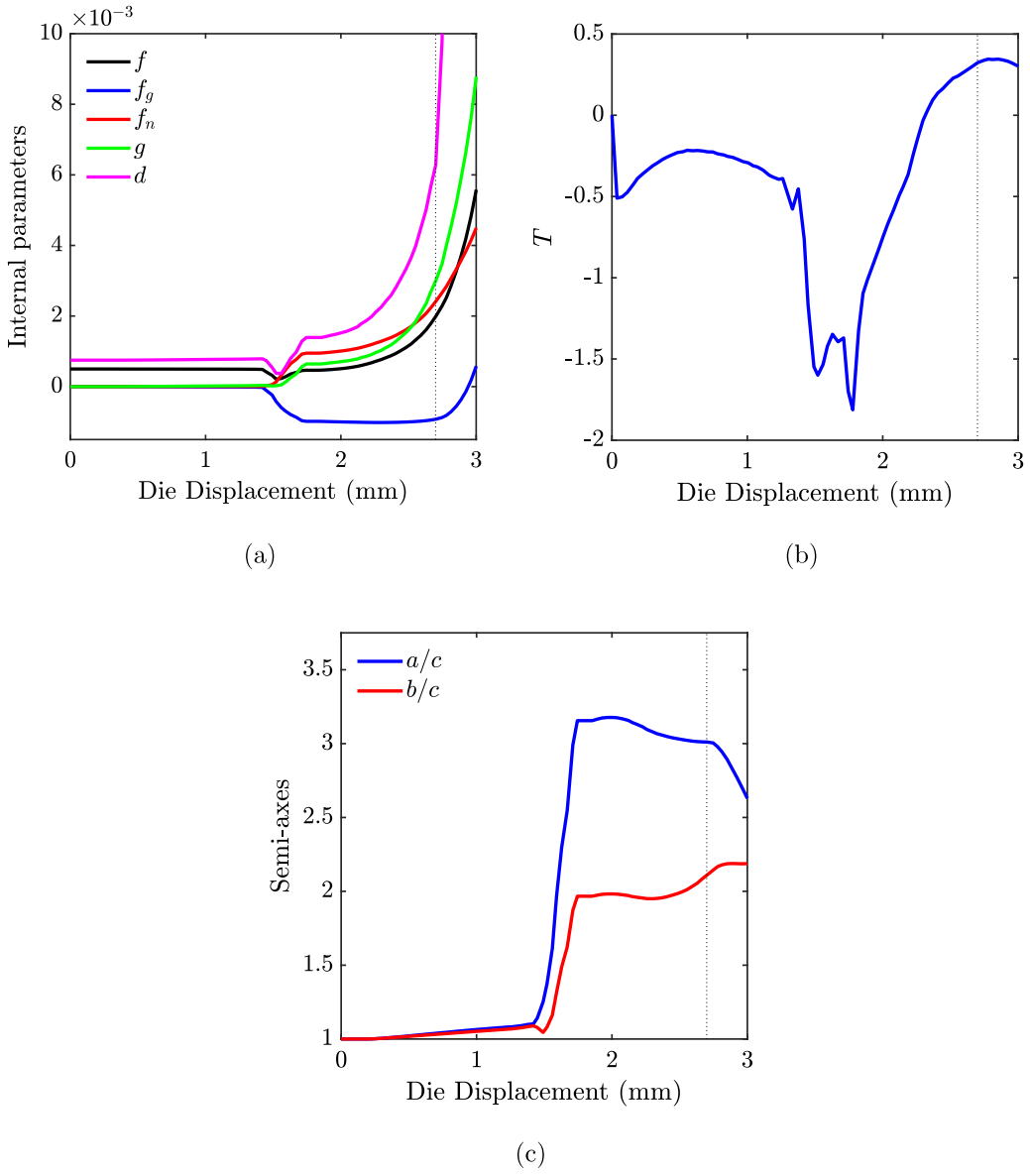

Fig. 22. Evolution of internal parameters in the integration point that fails first in the simulation of corrugation processing. (a) Damage parameter d, total porosity f, second porosity g, porosity due to nucleation f_n and porosity due to void growth f_g, (b) Stress triaxiality T and (c) Semi-axes a/c and b/c.

Then, the distribution of the damage parameter d is represented for several displacements of the corrugation die (2.8 mm, 3 mm and 3.3 mm which is the end of the simulation), and is compared to the fractured specimen in Fig. 20. Overall, the location of the crack and its 'cross' shape are well reproduced by the ML model during the simulation of the corrugation, by comparison with the photograph of the quasi-fractured specimen (taken on a pattern far from the boundaries). In the simulation, the damage parameter becomes localized with very high values (higher than 0.2) for a displacement of about 3.3 mm which is in agreement with the experimental values.

In addition, the distribution of the porosity is represented in Fig. 21 for two displacements of the corrugation die (3 mm and 3.3 mm). It is localized in the same regions as the damage parameter but its maximal value is of about 0.02, which is ten times lower than the damage parameter. As in the case of deep drawing, from the definition of the damage parameter, this difference can be attributed by two factors, void shape effects and/or coalescence.

Then, the evolution of the total porosity f, second porosity g, nucleated porosity f_n, void growth porosity f_g, stress triaxiality T and semi-axes ratios a/c and b/c are represented (versus the punch displacement) in Fig. 22 in the element that fails first, in order to understand the effect of each mechanism on the failure. Before that coalescence occurs (for a corrugation die displacement lower than 2.7 mm), the porosity due to void growth (f_g) decreases while the porosity due to void nucleation (f_n) increases; before a die displacement of 2 mm, the total porosity is almost constant and then it slightly increases due to void nucleation. The second porosity (g), related to void shape effects, increases with a rate similar to the total porosity. Therefore, in the case of corrugation, the ML model predicts no void growth, and the increase of the quantity $(f + g)$ is mainly due to void shape effects (through g) and void nucleation (through f_n). The stress triaxiality T is negative before coalescence which explains void closure. As shown in Fig. 22c, important void shape effects are associated with the increase of the second porosity; before coalescence, the maximal values for the semi axes are of about $a/c \sim 3$ and $b/c \sim 2$. The initial spherical void thus becomes a general ellipsoidal cavity. It must be noted that the element which fails first is located under the upper side of the pointy edge of the corrugation die; hence during the beginning of the process (before 1.5 mm of die displacement) it is slightly deformed. This explains why

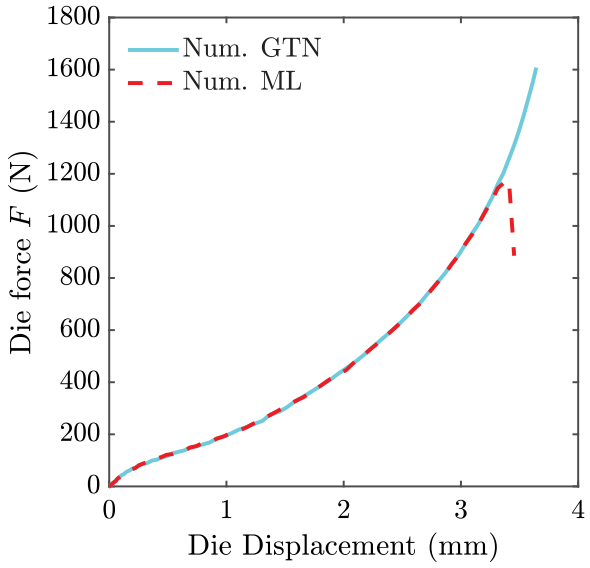

Fig. 23. Comparison of the die force–displacement curves using ML and GTN in the case of corrugation processing.

the internal parameters do not evolve much before a displacement of 1.5 mm.

5.3. Comparison with Gurson's model

The simulation of the corrugation process is now investigated using Gurson's model without void shape effects. In that case, the same set of parameters (see Table 7) was used because it was found to reproduce accurately the tensile test using the GTN model.

The force–displacement curves of the corrugation die using Gurson's model are compared to that obtained with ML model and to the experimental results, in Fig. 23. Overall, the force–displacement curve is very similar using both GTN and ML models before the occurrence of softening. The simulation ends for a displacement of about 3.7 mm using the GTN model but in this case the numerical instability is not associated with a macroscopic softening on the force–displacement curve.

The distribution of the porosity is represented in Fig. 24 for two values of the corrugation die displacement (3.3 mm and 3.7 mm). At a displacement of 3.3 mm (for which failure is observed experimentally) the distribution of the porosity follows the 'cross-shape' but it is not localized enough to trigger macroscopic softening. Then, at a displacement of about 3.7 mm (for which the simulation ends), the distribution of the porosity in that case is similar to the shape of the crack in the experiments although it is localized in very small areas which were not observed experimentally. The maximum level of the porosity is about 0.02 which approximately corresponds to $f^* \approx 0.0975$.

Therefore, given that (i) the displacement leading to failure is overestimated, (ii) no softening is observed on the macroscopic force–displacement curve and (iii) the crack morphology is not similar to that observed experimentally, it cannot be concluded that failure is quantitatively predicted using Gurson's model.

6. Discussion

The ML model has permitted to reproduce several macroscopic features observed in forming processes involving complex loading paths with local shear-dominated states. Those results, together with those previously obtained on shear-dominated butterfly specimens (Morin et al., 2017a) and on micromechanical cell calculations (Morin et al., 2016), confirm the capabilities of the ML model to predict ductile failure at low stress triaxialities in presence of intense shear. Therefore, this model can be considered as an alternative to uncoupled models for the simulation of forming processes because it can predict crack propagation. Indeed, even though uncoupled models are interesting to provide the strain-to-failure (Gorji and Mohr, 2018), this class of models cannot predict crack propagation since they do not take into account the loading history of the damage variables. Furthermore, the ML model can also be considered as a viable micromechanical alternative to Nahshon and Hutchinson (2008)'s modification of Gurson's model for the simulation of forming processes. Indeed, even though Nahshon and Hutchinson (2008)'s model was successfully applied to the prediction of punch tests (Ying et al., 2018), this model is based on a heuristic modification of the evolution equation of the porosity, which is not identical to the true volume fraction of the voids, but can be interpreted as a heuristic damage parameter. Consequently, a notable advantage of the ML model is that softening in shear is not due to an artificial increase of the porosity as it is the direct consequence of void shape effects (with possible void closure)

This work constitutes an important first step toward the simulation of complex processing routes involved in forming processing using Gurson-type models. It must be noted that the good agreement observed between experiments and simulations could be improved by refining the model in the following directions:

- The model of coalescence considered in this work is based on Tvergaard and Needleman (1984)'s classical modification of Gurson's model in which the parameter $(f + g)$ in the criterion is artificially increased when it reaches some critical value $(f + g)_c$. Although this simple heuristic model is generally considered sufficient to describe the coalescence regime, it requires the calibration of the critical value $(f+g)_c$ which does not have a physical interpretation. The development of a micromechanical model of coalescence for general ellipsoidal cavities including shear effects, following Torki and Benzerga (2018)'s direction, would be necessary to improve the prediction of failure in shear-dominated loadings.
- The final shape of a product obtained after forming is generally linked to the plastic material flow. Plastic anisotropy is important as it explains notably undulated rims called ears in deep drawing (see e.g. Liu et al. (2020)). The extension of this work to plastic anisotropy is thus necessary to simulate more precisely sheet forming processes. This can be done by considering (i) plastic anisotropy directly in the limit-analysis procedure as done by Morin et al. (2015) who extended the ML model to a quadratic Hill's matrix, or (ii) induced plastic anisotropy in the mechanical response through the evolution of crystallographic texture at several scales as done by Paux et al. (2020) and Frodal et al. (2021).
- The corrugation process in this work has been performed using an aluminum alloy 7075-T6 for which failure occurs during the first step of corrugation. In practical applications, RCS processing should be performed with more ductile materials in order to repeat several passes to provide grain refinement: for instance with a 5754 Al alloy, four passes can be achieved (Ezequiel et al., 2020) before fracture.[3] In such case, since several passes are repeated, it would be necessary to consider cyclic effects on plasticity such as kinematic hardening. Recently, Gurson's model for spherical void was extended to kinematic using sequential limit-analysis (Morin et al., 2017b), but the derivation of a general model which combines local kinematic hardening and ellipsoidal voids remains to be done.

[3] Interestingly, with an annealed aluminum alloy 7075-T6, four RCS passes can be reached (Romero-Resendiz et al., 2021), which suggests that the effect of the initial microstructure is important in the occurrence of damage and should be included in the ML model.

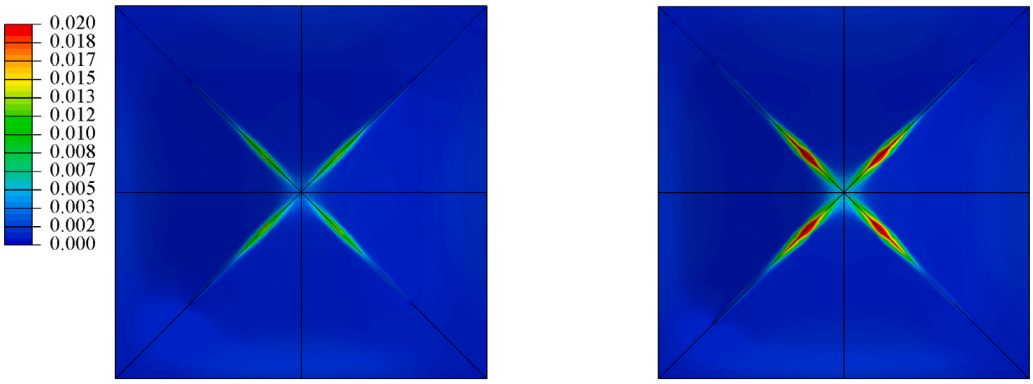

Fig. 24. Distribution of the porosity using the GTN model in the simulation of the corrugation process. (a) Die displacement of 3.3 mm and (b) Die displacement of 3.7 mm.

- The coupling between damage and the elastic properties is generally not taken into account in Gurson-type models (including the ML model) which constitutes a disadvantage of this approach compared to CDM-type models (Saanouni et al., 2000). This could be approximately accounted for through some homogenization scheme for the elastic properties that would depend on the void morphology, as done by Dorhmi et al. (2020) in the case of spherical metal–matrix composites using a two-step homogenization in which the volume fractions affect the elastic properties that are described by Mori–Tanaka's model. This would permit to assess the effect of forming on the possible stiffness loss.

7. Conclusion

The aim of this work was to investigate and predict ductile failure in forming processing. Experimental results of deep drawing and corrugation processing on aluminum alloys have shown that ductile failure in forming processes can be the consequence of shear-dominated loadings. In the case of deep drawing, several modes of cracking are observed depending on the blank size. In corrugation processing, a crack is observed in regions subjected to intense shear. In order to simulate those experiments, the Madou–Leblond model, which is an extension of Gurson's model incorporating void shape effects, has been considered. In the case of deep drawing, this model permits to reproduce 'bottom cracks' for large blanks and 'shear cracks' for small blanks. The evolution of the internal parameters of the ML model has permitted to highlight the importance of void shape effects upon the final failure. When the triaxiality is low, the porosity decreases but the ratios between the void's semi-axes increase which leads to some softening: indeed in this model, softening can be induced by void shape effects through the second porosity. In the case of corrugation processing, the ML model has permitted to reproduce accurately the occurrence of failure as well as the shape of the crack. In that case also, void shape effects are important in the region that fails first. Finally, comparisons with the GTN for both processes show its difficulty to simulate accurately failure because it generally overestimates ductility since it disregards void shape effects.

Declaration of competing interest

The authors declare that they have no known competing financial interests or personal relationships that could have appeared to influence the work reported in this paper.

Acknowledgments

Fruitful discussions with D. Mohr are gratefully acknowledged. G.G. acknowledges UNAM-DGAPA-PASPA, Mexico program for funding the sabbatical year at the UPV.

References

Ablat, M.A., Qattawi, A., 2017. Numerical simulation of sheet metal forming: a review. Int. J. Adv. Manuf. Technol. 89, 1235–1250.
Badreddine, H., Labergère, C., Saanouni, K., 2016. Ductile damage prediction in sheet and bulk metal forming. C. R. Méc. 344, 296–318.
Banabic, D., 2010. Sheet Metal Forming Processes: Constitutive Modelling and Numerical Simulation. Springer-Verlag, Berlin Heidelberg.
Barsoum, I., Faleskog, J., 2007. Rupture mechanisms in combined tension and shear—Experiments. Int. J. Solids Struct. 44, 1768–1786.
Benseddiq, N., Imad, A., 2008. A ductile fracture analysis using a local damage model. Int. J. Press. Vessels Pip. 85, 219–227.
Benzerga, A.A., 2002. Micromechanics of coalescence in ductile fracture. J. Mech. Phys. Solids 50, 1331–1362.
Benzerga, A.A., Besson, J., 2001. Plastic potentials for anisotropic porous solids. Eur. J. Mech. A Solids 20, 397–434.
Benzerga, A.A., Leblond, J.B., 2010. Ductile fracture by void growth to coalescence. Adv. Appl. Mech. 44, 169–305.
Benzerga, A.A., Leblond, J.B., 2014. Effective yield criterion accounting for microvoid coalescence. J. Appl. Mech. 81, 031009.
Benzerga, A.A., Leblond, J.B., Needleman, A., Tvergaard, V., 2016. Ductile failure modeling. Int. J. Fract. 201, 29–80.
Besson, J., 2010. Continuum models of ductile fracture: A review. Int. J. Damage Mech. 19, 3–52.
Bong, H.J., Kim, D., Kwon, Y.N., Lee, J., 2021. Predicting hot deformation behaviors under multiaxial loading using the Gurson-Tvergaard-Needleman damage model for Ti–6al–4v alloy sheets. Eur. J. Mech. A Solids 87, 104227.
Bonora, N., 1997. A nonlinear CDM model for ductile failure. Eng. Fract. Mech. 58, 11–28.
Cai, Z.Y., Meng, B., Wan, M., Wu, X.D., Fu, M.W., 2020. A modified yield function for modeling of the evolving yielding behavior and micro-mechanism in biaxial deformation of sheet metals. Int. J. Plast. 129, 102707.
Chu, C.C., Needleman, A., 1980. Void nucleation effects in biaxially stretched sheets. J. Eng. Mater. Technol. 102, 249–256.
Dorhmi, K., Morin, L., Derrien, K., Hadjem-Hamouche, Z., Chevalier, J.P., 2020. A homogenization-based damage model for stiffness loss in ductile metal–matrix composites. J. Mech. Phys. Solids 137, 103812.
Dunand, M., Mohr, D., 2011a. On the predictive capabilities of the shear modified Gurson and the modified Mohr–Coulomb fracture models over a wide range of stress triaxialities and Lode angles. J. Mech. Phys. Solids 59, 1374–1394.
Dunand, M., Mohr, D., 2011b. Optimized butterfly specimen for the fracture testing of sheet materials under combined normal and shear loading. Eng. Fract. Mech. 78, 2919–2934.
Elizalde, S., Ezequiel, M., Figueroa, I.A., Cabrera, J.M., Braham, C., Gonzalez, G., 2020. Microstructural evolution and mechanical behavior of an Al-6061 alloy processed by repetitive corrugation and straightening. Metals 10, 489.
Enakoutsa, K., Leblond, J., Perrin, G., 2007. Numerical implementation and assessment of a phenomenological nonlocal model of ductile rupture. Comput. Methods Appl. Mech. Engrg. 196, 1946–1957.
Ezequiel, M., Figueroa, I.A., Elizalde, S., Cabrera, J.M., Braham, C., Morin, L., Gonzalez, G., 2020. Numerical and experimental study of a 5754-aluminum alloy processed by heterogeneous repetitive corrugation and straightening. J. Mater. Res. Technol. 9, 1941–1947.
Frodal, B.H., Thomesen, S., Børvik, T., Hopperstad, O.S., 2021. On the coupling of damage and single crystal plasticity for ductile polycrystalline materials. Int. J. Plast. 142, 102996.

Ghahremaninezhad, A., Ravi-Chandar, K., 2013. Ductile failure behavior of polycrystalline Al 6061-T6 under shear dominant loading. Int. J. Fract. 180, 23–39.
Gologanu, M., 1997. Etude de Quelques Problèmes de Rupture Ductile Des Métaux (Ph.D. thesis). Université Paris 6.
Gorji, M., 2015. Instability and Fracture Models to Optimize the Metal Forming and Bending Crack Behavior of Al-Alloy Composites (Ph.D. thesis). ETH-Züich.
Gorji, M., Berisha, B., Hora, P., Barlat, F., 2016a. Modeling of localization and fracture phenomena in strain and stress space for sheet metal forming. Int. J. Mater. Form. 9, 573–584.
Gorji, M., Berisha, B., Manopulo, N., Hora, P., 2016b. Effect of through thickness strain distribution on shear fracture hazard and its mitigation by using multilayer aluminum sheets. J. Mater Process. Technol. 232, 19–33.
Gorji, M.B., Mohr, D., 2018. Predicting shear fracture of aluminum 6016-T4 during deep drawing: Combining Yld-2000 plasticity with Hosford–Coulomb fracture model. Int. J. Mech. Sci. 137, 105–120.
Grolleau, V., Roth, C.C., Mohr, D., 2022. Design of in-plane torsion experiment to characterize anisotropic plasticity and fracture under simple shear. Int. J. Solids Struct. 236-237, 111341.
Gurson, A.L., 1977. Continuum theory of ductile rupture by void nucleation and growth: Part I–yield criteria and flow rules for porous ductile media. ASME J. Eng. Mater. Technol. 99, 2–15.
Haltom, S.S., Kyriakides, S., Ravi-Chandar, K., 2013. Ductile failure under combined shear and tension. Int. J. Solids Struct. 50, 1507–1522.
Kami, A., Dariani, B.M., Sadough Vanini, A., Comsa, D.S., Banabic, D., 2015. Numerical determination of the forming limit curves of anisotropic sheet metals using GTN damage model. J. Mater Process. Technol. 216, 472–483.
Kami, A., Dariani, B.M., Vanini, A.S., Comsa, D.S., Banabic, D., 2014. Application of a GTN damage model to predict the fracture of metallic sheets subjected to deep-drawing. Proc. Rom. Acad. Ser. A 15.
Leblond, J.B., 2015. UMAT available at the address www.dalembert.upmc.fr/home/leblond/.
Lemaitre, J., 1985. A continuous damage mechanics model for ductile fracture. J. Eng. Mater. Technol. 107, 83–89.
Liu, W., Chen, B.K., Pang, Y., Najafzadeh, A., 2020. A 3D phenomenological yield function with both in and out-of-plane mechanical anisotropy using full-field crystal plasticity spectral method for modelling sheet metal forming of strong textured aluminum alloy. Int. J. Solids Struct. 193–194, 117–133.
Madou, K., Leblond, J.B., 2012a. A gurson-type criterion for porous ductile solids containing arbitrary ellipsoidal voids—I: Limit-analysis of some representative cell. J. Mech. Phys. Solids 60, 1020–1036.
Madou, K., Leblond, J.B., 2012b. A gurson-type criterion for porous ductile solids containing arbitrary ellipsoidal voids—II: Determination of yield criterion parameters. J. Mech. Phys. Solids 60, 1037–1058.
Madou, K., Leblond, J.B., 2013. Numerical studies of porous ductile materials containing arbitrary ellipsoidal voids—I: Yield surfaces of representative cells. Eur. J. Mech. A Solids 42, 480–489.
Madou, K., Leblond, J.B., Morin, L., 2013. Numerical studies of porous ductile materials containing arbitrary ellipsoidal voids—II: Evolution of the length and orientation of the void axes. Eur. J. Mech. A Solids 42, 490–507.
Morin, L., Leblond, J.B., Kondo, D., 2015. A Gurson-type criterion for plastically anisotropic solids containing arbitrary ellipsoidal voids. Int. J. Solids Struct. 77, 86–101.
Morin, L., Leblond, J.B., Mohr, D., Kondo, D., 2017a. Prediction of shear-dominated ductile fracture in a butterfly specimen using a model of plastic porous solids including void shape effects. Eur. J. Mech. A Solids 61, 433–442.
Morin, L., Leblond, J.B., Tvergaard, V., 2016. Application of a model of plastic porous materials including void shape effects to the prediction of ductile failure under shear-dominated loadings. J. Mech. Phys. Solids 94, 148–166.
Morin, L., Michel, J.C., Leblond, J.B., 2017b. A Gurson-type layer model for ductile porous solids with isotropic and kinematic hardening. Int. J. Solids Struct. 118, 167–178.
Nahrmann, M., Matzenmiller, A., 2021. Modelling of nonlocal damage and failure in ductile steel sheets under multiaxial loading. Int. J. Solids Struct. 232, 111166.
Nahshon, K., Hutchinson, J.W., 2008. Modification of the Gurson model for shear failure. Eur. J. Mech. A Solids 27, 1–17.
Nielsen, K.L., Dahl, J., Tvergaard, V., 2012. Collapse and coalescence of spherical voids subject to intense shearing: studied in full 3d. Int. J. Fract. 177, 97–108.
Pack, K., Tancogne-Dejean, T., Gorji, M.B., Mohr, D., 2018. Hosford-Coulomb ductile failure model for shell elements: Experimental identification and validation for DP980 steel and aluminum 6016-T4. Int. J. Solids Struct. 151, 214–232.
Pandya, K.S., Roth, C.C., Mohr, D., 2020. Strain rate and temperature dependent fracture of aluminum alloy 7075: Experiments and neural network modeling. Int. J. Plast. 135, 102788.
Paux, J., Ben Bettaieb, M., Badreddine, H., Abed-Meraim, F., Labergere, C., Saanouni, K., 2020. An elasto-plastic self-consistent model for damaged polycrystalline materials: Theoretical formulation and numerical implementation. Comput. Methods Appl. Mech. Engrg. 368, 113138.
Pineau, A., Benzerga, A.A., Pardoen, T., 2016. Failure of metals I: Brittle and ductile fracture. Acta Mater. 107, 424–483.
Ponte Castañeda, P., Zaidman, M., 1994. Constitutive models for porous materials with evolving microstructure. J. Mech. Phys. Solids 42, 1459–1497.
Romero-Resendiz, L., Amigó-Borrás, V., Vicente-Escuder, A., Elizalde, S., Cabrera, J.M., Pineda-Ruiz, D., Figueroa, I.A., Gonzalez, G., 2021. Effect of the microstructure generated by repetitive corrugation and straightening (RCS) process on the mechanical properties and stress corrosion cracking of al-7075 alloy. J. Mater. Res. Technol. 15, 4564–4572.
Roth, C.C., Morgeneyer, T.F., Cheng, Y., Helfen, L., Mohr, D., 2018. Ductile damage mechanism under shear-dominated loading: In-situ tomography experiments on dual phase steel and localization analysis. Int. J. Plast. 109, 169–192.
Saanouni, K., 2006. Virtual metal forming including the ductile damage occurrence: Actual state of the art and main perspectives. J. Mater Process. Technol. 177, 19–25.
Saanouni, K., 2008. On the numerical prediction of the ductile fracture in metal forming. Eng. Fract. Mech. 75, 3545–3559.
Saanouni, K., Nesnas, K., Hammi, Y., 2000. Damage modeling in metal forming processes. Int. J. Damage Mech. 9, 196–240.
Saxena, R.K., Dixit, P.M., 2011. Numerical analysis of damage for prediction of fracture initiation in deep drawing. Finite Elem. Anal. Des. 47, 1104–1117.
Soyarslan, C., Tekkaya, A.E., 2010. A damage coupled orthotropic finite plasticity model for sheet metal forming: CDM approach. Comput. Mater. Sci. 48, 150–165.
Springmann, M., Kuna, M., 2005. Identification of material parameters of the Gurson–Tvergaard–Needleman model by combined experimental and numerical techniques. Comput. Mater. Sci. 33, 501–509.
Tajdary, P., Morin, L., Braham, C., Gonzalez, G., 2021. A reduced single-pattern model for the numerical simulation of multi-pattern metal forming. Int. J. Mater. Form. 14, 1403–1416.
Teixeira, P., Santos, A.D., Andrade Pires, F.M., César de Sá, J.M.A., 2006. Finite element prediction of ductile fracture in sheet metal forming processes. J. Mater Process. Technol. 177, 278–281.
Tekkaya, A.E., Bouchard, P.O., Bruschi, S., Tasan, C.C., 2020. Damage in metal forming. CIRP Ann. 69, 600–623.
Thuillier, S., Maire, E., Brunet, M., 2012. Ductile damage in aluminium alloy thin sheets: Correlation between micro-tomography observations and mechanical modeling. Mater. Sci. Eng. A 558, 217–225.
Torki, M.E., Benzerga, A.A., 2018. A mechanism of failure in shear bands. Extreme Mech. Lett. 23, 67–71.
Tvergaard, V., 1981. Influence of voids on shear band instabilities under plane strain conditions. Int. J. Fract. 17, 389–407.
Tvergaard, V., Needleman, A., 1984. Analysis of the cup-cone fracture in a round tensile bar. Acta Metall. 32, 157–169.
Uthaisangsuk, V., Prahl, U., Münstermann, S., Bleck, W., 2008. Experimental and numerical failure criterion for formability prediction in sheet metal forming. Comput. Mater. Sci. 43, 43–50.
Yang, Z., Zhao, C., Dong, G., Chen, Z., 2021. Experimental calibration of ductile fracture parameters and forming limit of AA7075-T6 sheet. J. Mater Process. Technol. 291, 117044.
Ying, L., Wang, D.t., Liu, W.q., Wu, Y., Hu, P., 2018. On the numerical implementation of a shear modified GTN damage model and its application to small punch test. Int. J. Mater. Form. 11, 527–539.
Zhang, K., Badreddine, H., Yue, Z., Hfaiedh, N., Saanouni, K., Liu, J., 2021. Failure prediction of magnesium alloys based on improved CDM model. Int. J. Solids Struct. 217–218, 155–177.
Zhang, L., Min, J., Carsley, J.E., Stoughton, T.B., Lin, J., 2017. Experimental and theoretical investigation on the role of friction in Nakazima testing. Int. J. Mech. Sci. 133, 217–226.
Zhang, Z., Wu, Y., Huang, F., 2022. Extension of a shear-controlled ductile fracture criterion by considering the necking coalescence of voids. Int. J. Solids Struct. 236–237, 111324.